The Astrophysical Journal, 693:186–206, 2009 March 1 doi:10.1088/0004-637X/693/1/186

ON THE DYNAMICAL EVOLUTION OF H II REGIONS: AN INVESTIGATION OF THE IONIZED COMPONENT OF W4, A GALACTIC CHIMNEY CANDIDATE. II. KINEMATICS AND DYNAMICS IN THE LATITUDE RANGE $3^\circ < b \leqslant 7^\circ$

Dominic Lagrois and Gilles Joncas
Département de physique, de génie physique et d'optique, Centre de Recherche en Astrophysique du Québec, Université Laval, Québec, QC G1K 7P4, Canada;
dominic.lagrois.1@ulaval.ca, joncas@phy.ulaval.ca
Received 2008 July 22; accepted 2008 November 11; published 2009 February 27

ABSTRACT

In the second of this two-paper series, we present results associated with an Hα investigation, obtained using the Fabry–Perot interferometer FaNTOmM, of the tenuous ionized material found embedded in the northern portion of W4. W4 is a promising candidate for a galactic chimney, likely connected with the galactic corona, and presents evidence of shell fragmentation. We present the quantitative method for identifying shell breakout that allows us to characterize the giant H I supershell/H II region W4 as enclosing a galactic chimney in formation. On a range of approximately 125 pc, two "south-to-north" radial velocity gradients are detected, $\nabla_v = (-)0.17$ km s^{-1} pc^{-1} ($3\overset{\circ}{.}5 \leqslant b < 6\overset{\circ}{.}3$) and $\nabla_v = (-)3.13$ km s^{-1} pc^{-1} ($6\overset{\circ}{.}3 \leqslant b \leqslant 6\overset{\circ}{.}5$). This leads to radial velocities, slightly above the vicinity of the shell's polar cap, of -70 km s^{-1}, blueshifted by nearly 25 km s^{-1} with respect to the H I supershell. The kinematic behavior is in agreement with a rarefaction scenario if the W4 superbubble presents a tilt toward the observer. This angle of inclination is estimated between 9° and 27° with respect to the plane of the sky. A line-narrowing gradient is correlated with the radial velocity gradient. The large-scale trends in radial velocities and line widths correspond to highly accelerated, well-parallelized outflows of vented ionized material. This kinematic signature is expected from the chimney model. The dynamical age of the W4 chimney is estimated at 4.1 Myr and constraints shell instabilities to have developed at latitudes lower than the blowout threshold height. Our work contributes to the evidence that the star cluster IC 1805 partially sustains the low-galactic corona above the Perseus arm.

Key words: Galaxy: halo – ISM: bubbles – ISM: individual (W4) – ISM: kinematics and dynamics – techniques: interferometric

1. INTRODUCTION

The implication of galactic chimneys (Norman & Ikeuchi 1989) in the sustainment of the hot, ionized galactic corona has been investigated for the past three decades. Numerical models have shown the formation of ovoid supershells fueled by the action of supernova explosions (Chevalier & Gardner 1974), the mechanical deposit of Lyα radiation (Dove et al. 2000) and stellar winds (Basu et al. 1999) of large star clusters. Assuming an exponentially decreasing galactic atmosphere model (Dickey & Lockmann 1990; Heiles 1991), blowout events occur once the polar cap of an expanding supershell overtakes the galactic layer of neutral material. According to Mac Low et al. (1989), the blowout threshold is estimated at 2 to 3 times the vertical scale height of the H I distribution above mid-plane. There is a dramatic drop in particle density and pressure from the upstream interstellar medium (hereafter, ISM). This, in turn, leads to a sudden acceleration of the shell's polar cap segment. Dove et al. (2000) proposed this particular scenario as ideal for fast shell instability development, which is responsible for shell weaknesses and ultimately fracture. Shell openings, therefore, assure that a certain fraction of the energetic photons will exit the H II region. The evacuated photons will likely travel to interact with the galactic corona contributing to the sustainment of the Reynolds layer (Reynolds 1989a).

Observational identification of shell breakouts usually relies on visual aspects. An investigation using a more quantitative method is required especially for superbubbles displaying observational evidence for ionization-bounded supershells. Due to the pressure difference between the warm interior and the outer ISM, openings found on some supershell will likely vent interior gas outwards. Induced at the point of fracture, a rarefaction wave will quickly develop and sweep out a large amount of embedded ionized material. That is, a discontinuity associated with the wave will propagate from the fracture toward the center of the superbubble, while the gas that is being rarefied will move in the opposite direction, toward the fragmenting shell of the superbubble. The shocked material is accelerated through the "interior-to-exterior" pressure gradient before being evacuated. For gas flows not strictly parallel to the plane of the sky, a kinematic discrepancy can be established between the high-velocity-accelerated component, being evacuated, and the unperturbed material found deeper in the superbubble. This model particularly resembles the kinematics anticipated from the embedded air in a pierced metal container (see Section 5.2). The galactic superbubble/H II region W4 characterized by a slight tilt toward the observer (Normandeau et al. 1996) represents an ideal astronomical object to verify such a model.

In Section 2, we present the promising galactic chimney candidate W4. Large-scale observations have led to the detection of two possible breaks located along the northern shell frame. Techniques used for data acquisition and reduction are described in Section 3. We provide, in Section 4, the results of our Fabry–Perot Hα investigation in the northern portion of W4, bounded in latitude between 3° and 7°. Our model of a pierced metal container will be presented in Section 5 and used in the interpretation of the observed gas motion. A review of the most important results and conclusion will be presented in Section 6.

2. THE W4 SUPERBUBBLE

In our first paper (Lagrois & Joncas 2009, hereafter Paper I), we introduced the galactic wind-blown bubble/H II region W4 which was the central feature of the Canadian Galactic Plane Survey (CGPS) pilot project (Normandeau et al. 1997). Observations in the radio regime have presented W4 as an impressive H I cavity aiming toward the galactic corona and visible in the radial velocity range between −38.46 and −45.05 km s^{-1} as measured in the local standard of rest (hereafter, LSR) (West et al. 2007). Outflows from the star cluster IC 1805 (Shi & Hu 1999) were said to be responsible for the actual superbubble expansion (Basu et al. 1999). A northern extension of the CGPS spectroscopic 21 cm line observations, used in Paper I, is presented in Normandeau (2000). The H I supershell is seen extending between $b = 0°$ and $b = 6°$ and presents no evidence for a neutral polar cap at the northernmost latitudes (Normandeau 2000). From polarization observations, West et al. (2007) outlined a roughly egg-shaped supershell reaching a height of roughly 245 parsecs above the galactic mid-plane, considering a spectroscopic distance of 2.35 kpc to the star cluster (Massey et al. 1995). Considering the vertical scale height of the H I distribution estimated at 140 pc above the Perseus arm (Normandeau 2000), it is assumed that the shell's polar region is located slightly below the blowout threshold and should not, therefore, show signs of a re-accelerated expansion.

Dennison et al. (1997) obtained a large-scale view of the Hα emission associated with the W4 H II region. The 10° circular field of view (FOV) revealed an ionized counterpart to the H I supershell. The neutral shell is apparently eroded from its inner side. The shell can, therefore, be referred as being semi-neutral, semi-ionized. A faint ionized polar cap seems to be detected roughly 230 pc above the galactic mid-plane. Even though the outer shock wave of the expanding structure left very little material behind it, a diffuse ionized component is observed embedded in the superbubble. In Paper I, partial sources of material were identified as numerous and mostly molecular blobs found either inside or at the periphery of the supershell and exposed to the UV flux of the nearby star cluster. Generally located at low-galactic latitude, these eroded features contributed to establish a discrepancy in emissivity between what we referred as the southern ($0° \leqslant b \leqslant 3°$, hereafter W4-south) and northern ($3° < b \leqslant 7°$, hereafter W4-north) portions of W4 respectively made up of strong and faint Hα emission. This paper will mainly focus on the description and the kinematic investigation of W4-north.

At the boundary between W4-south and -north, slightly bended neutral filaments (hereafter, referred to the "H I horizontal sheets") are detected, covering in longitude an important fraction of the bubble's width. A second, but nonetheless important, atomic feature is observed near the shell's polar cap. Kinematically linked to the H I supershell, the intriguing vertical H I-spur (Normandeau 2000) is highly similar to worm-like structures obtained from numerical models of accelerated wind-blown bubbles and interpreted as filamentary remnants of unstable broken shells (De Avillez & Berry 2001). In fact, the investigation of the large-scale Hα (Dennison et al. 1997) and 1420/408 MHz continuum (CGPS) emissions has revealed particularly faint shell material in the direct vicinity of the H I spur (West 2003; West et al. 2007). The authors interpreted the lack of emission as an observational evidence for a recent shell fracture. A second possible break is also detected along the western side of the W4 supershell. Combined with a lack of high-latitude ionizing photons (Terebey et al. 2003) and of erodible neutral clumps, dramatic gas venting might have deprived W4-north of its emissive material; all contributing to the discrepancy in emissivity between the two portions of the nebula. In order to visualize the location of each feature, the reader is referred to the schematic drawing of W4-north in Figure 1.

On a much larger scale of view, the Wisconsin Hα Mapper (WHAM) Northern Sky Survey (Reynolds et al. 2001) has revealed a large horseshoe-shaped Hα loop above the W3/W4/W5 complex, at a relatively low-galactic corona level (about 1 kpc above galactic mid-plane). Striking similarities can be established between the bent H I capped structures observed above the known chimney associated with the galactic supershell GSH 242-03+37 (McClure-Griffiths et al. 2006) and the giant ionized loop (hereafter, referred as the "Reynolds loop"). Mostly due to a remarkable alignment between the W4 superbubble and the Reynolds loop, Reynolds et al. (2001) proposed its sustainment to be partially attributed to the star cluster IC 1805.

In order to investigate the percolation of energetic photons through the possible shell breakouts, Hα observations via Fabry–Perot interferometry were carried out on the tenuous embedded material of W4-north. Since a strong disagreement exists (H I versus Hα and polarization observations) regarding a possible polar cap, our own work becomes crucial to assess whether the W4 superbubble is a chimney or not. Our motivation is based on our model of a pierced metal container and the expected large-scale radial velocity gradients directed toward the shell openings. Such gradients, associated with gas venting outwards, have remained undetected in our kinematic investigation of W4-south in Paper I due to a "north-to-south" sound crossing time of the nebula estimated at 25 Myr, well above the proposed dynamical age of the superbubble (Dennison et al. 1997). Therefore, rarefaction waves emanating from unstable northern-shell segments and propagating in a roughly sonic regime would still be found well above $b = 3°$, leaving unperturbed the ionized material found in the vicinity of the star cluster. Additionally, a northern portion of W4 mostly dominated by accelerated outflows of ejected material would confirm the formation of a galactic chimney and an obvious interaction between the star cluster IC 1805 and the Reynolds loop.

3. OBSERVATIONS AND DATA REDUCTION

Hα observations of W4-north were performed in 2006 and 2007 using the Ritchey–Chrétien 1.6 m telescope of the Observatoire du mont Mégantic (OmM). Similar to Paper I, the FaNTOmM (Fabry–Perot of New Technology for the Observatoire du mont Mégantic) device system was again used for data gathering. Technical information about the ultrasensitive IPCS camera can be found in Hernandez et al. (2003). The central interference order of the Fabry–Perot interferometer (hereafter, FPI) was fixed at 765 for a free spectral range of 8.56 Å centered on the Hα rest frequency. The finesse of the FPI varied slightly from night to night between 18 and 19. This allowed us to perform the spectral scanning at a fixed number of 44 steps (channels). All Hα emission spectra, therefore, presented a spectral resolution of 0.19 Å $channel^{-1}$ (or 8.89 km s^{-1} $channel^{-1}$). The λ6598.95 Ne line was used to produce interferograms for the radial velocity calibration, while narrow-band ($\Delta\lambda_{FWHM} = 10$ Å) filters allowed to isolate Hα lines from other ionized emission. Interference filters were chosen approximately in order to maximize flux transmission, that is, to

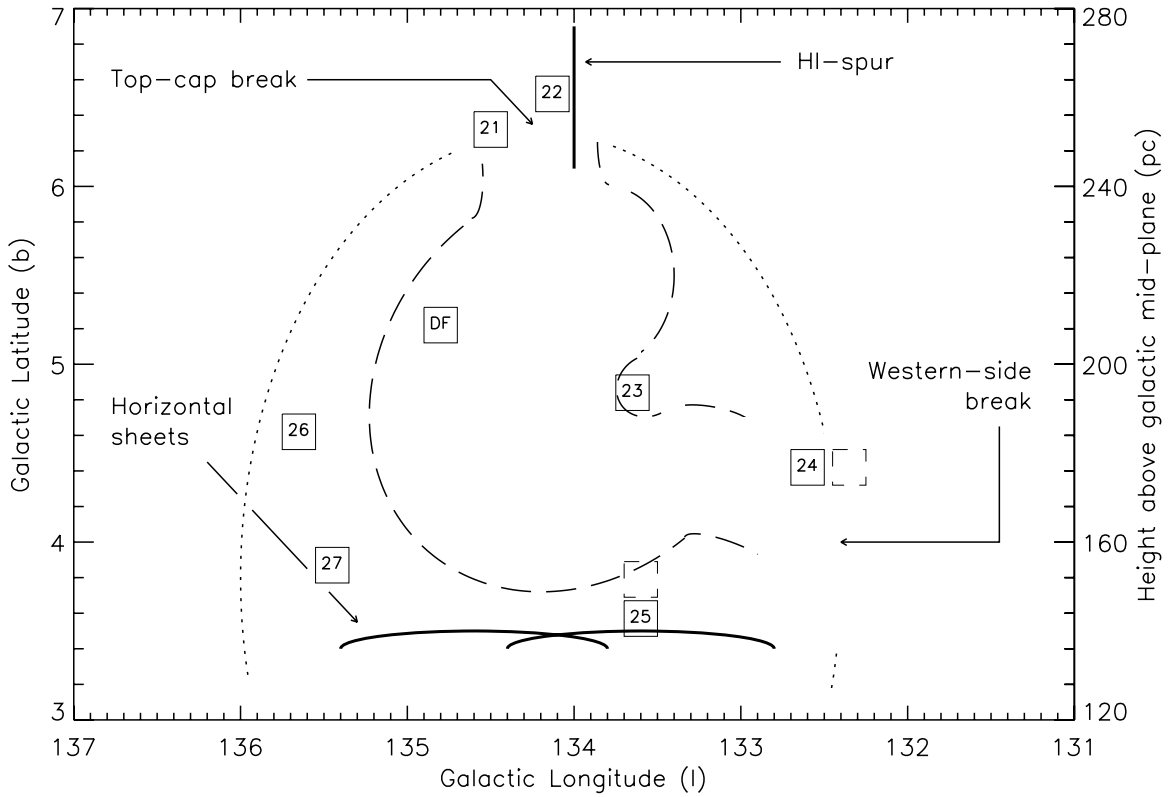

Figure 1. Schematic diagram of W4-north. The numbers coincide with the optical centers of the seven observed fields. The field labeled "DF" coincides with the location of the Dark Field used for night-sky subtraction. Bounded boxes enclose the FOV obtained from the FaNTOmM device system. The right-hand vertical axis shows the height above galactic mid-plane, assuming a spectroscopic distance of 2.35 kpc to the star cluster IC 1805. Atomic hydrogen features are represented by the bold solid lines. The long-dashed line encloses the $2^\circ \times 2^\circ$ portion inside the W4 superbubble where the Hα and 1420/408 MHz continuum emissions are seen particularly low (referred as the Hα-poor cavity in the text). The dotted line is related to the semi-neutral, semi-ionized W4 supershell. Dashed line "empty fields" near Fields 24 and 25 correspond to areas that remain to be investigated in order to perfectly interpret the kinematics of W4-north.

consider the effect of blueshifting (-0.2 Å K^{-1}) on transmission caused by cold ambient temperatures and to minimize the inclination of the different filters.

The use of the Panoramix f/2 focal reducer (Godbout et al. 1998) allowed us to obtain a square $12\farcm3 \times 12\farcm3$ FOV for a spatial resolution of $1\farcs45$ pixel^{-1} using the hard binned 512 × 512 80 frames s^{-1} mode of the CCD detector. Data reduction was carried out using IDL (Interactive Data Language) procedure (Daigle et al. 2006) specially tailored to reproduce the method used for the TAURUS FP spectrometer (Atherton et al. 1982).

We emphasized, in Paper I, the difficulty arising from night-sky emission (Osterbrock et al. 1996). The problem was partially eliminated by applying a multi-component Gaussian fit to each emission spectrum. The method demands each spectral line to be clearly identifiable in each raw spectrum. However, this criterion does not hold in spatial regions above the H I horizontal sheets, where the W4 Hα component is highly dominated by the emissivity of the Earth's mesosphere.

In order to mitigate the problem of night-sky emission, we use a semi-parallel procedure of sky subtraction that allows us to extract, from highly contaminated spectra, extremely faint W4 Hα profiles. The problem of sky subtraction must initially be treated as dual, being both spatial and temporal. Skinner et al. (1998) brilliantly demonstrated the optical variability of the night-sky emission as being dependent on the pointing position and the local time of the observations. In particular, the authors pointed out that the photometric properties of the sky vary on periods as short as 15 minute. Since the Hα emission from W4 fills our FOV, a patch of sky essentially devoided of emission was needed near the targeted areas. Examination of Figure 12 from West et al. (2007) shows a $2^\circ \times 2^\circ$ ionized gas trough centered on $(l, b) = (134\fdg5, 4\fdg9)$. This area is pictured in our Figure 1 using a long-dashed line and will be referred as the Hα-poor cavity. The small region labeled "DF," for Dark Field, was observed repeatedly during the night to measure the night-sky contamination. The sky subtraction scheme is shown in Figure 2. The angular separation between the Dark Field and individual W4 fields is $\gtrsim 1^\circ$ and the telescope was moved back and forth between W4 and DF. A given cycle, either associated with W4 or DF, corresponds to a one-time scanning of the 60 Å-wide wavelength interval (see Paper I). Each cycle is completed in ∼7 minute. Hence less than 15 minute elapses between two consecutive cycles, each Dark Field cycle labeled "j" can be subtracted from its associated W4 field cycle "j+1" (see Figure 2). From each DF subtracted observation, a faint but uncontaminated Hα profile is extracted. The procedure is repeated from $j = 1$ to $M - 1$ (W4 field cycle 01 and DF cycle M are naturally rejected from the procedure). The resulting Hα profiles are all summed in order to show a clear, high signal-to-noise ratio (hereafter, S/N), detection of the ionized material in W4-north. Once sky subtraction was completed, a Gaussian-fitting routine allowed us to extract, from each profile, the centroid position (radial velocity), the observed line width value (dispersion), and the amplitude of the fitted line. The M value for each W4 field (Figure 1) is listed in Table 1 (see Section 4).

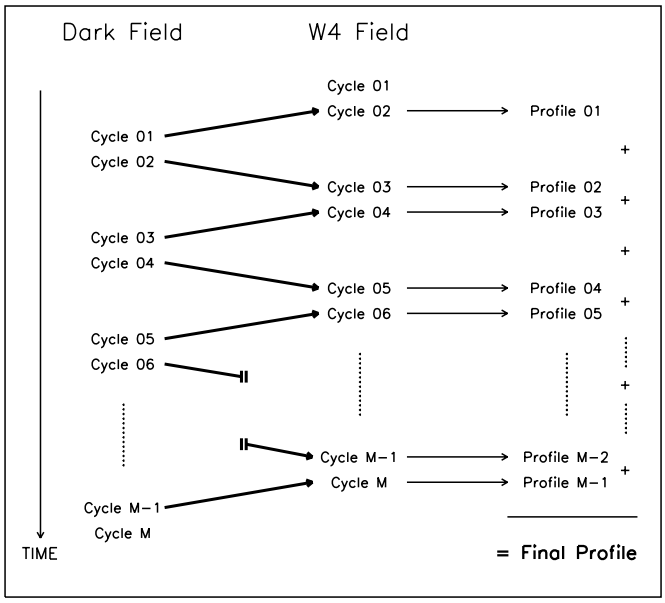

Figure 2. Schematic diagram of the night-sky subtraction method used during the observations and data reduction. Each cycle corresponds to an exposure time of ∼7 min. The total number of cycles gathered for each field (Dark and W4) is labeled "M." Cycles 01 and M, respectively for the W4 Field and the Dark Field, were rejected in every case. Solid thick arrows are to be translated as "... subtracted from...". The method is duplicated for every spatial pixel of the raw data cubes.

4. KINEMATICAL RESULTS

We present the large-scale kinematic behavior of the ionized component associated with W4-north. The schematic diagram of Figure 1 indicates the location of the FPI observations. A total of seven fields were obtained in order to detect the anticipated signature related to our model of a pierced metal container (that is the kinematic impact on the embedded ionized material attributed to rarefaction waves originating from the possible top-cap and western-side breaks). In order to pursue the terminology used for W4-south in Paper I, the new Hα observations were labeled from 21 to 27. The observations were carried out in order to investigate four specific areas of W4-north: the top-cap break (Fields 21, 22, and 23), the western-side break (Field 24), the H I horizontal sheets (Field 25), and the high-latitude W4 eastern wall (Fields 26 and 27). Each investigated area will be related to a particular subsection in Section 5.

Since the Hα emission is very faint, spatial binning was necessary in order to obtain significant S/Ns. Each field was spatially degraded to produce 4×4 pixel^2 raw data cubes before proceeding to sky subtraction (except for Field 26, observed in poor meteorological conditions, where a 2×2 pixel^2 cube produced better results). The number of points available, to establish a reliable kinematic model of W4-north, is, therefore, reduced to less than a 100. Figures 3–9 present the resulting three-dimensional cubes respectively for Fields 21 to 27. Each panel (i.e. pixel) corresponds to a 2.1×2.1 pc^2 area at the distance of W4 (4.2×4.2 pc^2 in Figure 8). The data points are represented by open circles. Gaussian fits to the observed W4 Hα profiles correspond to bold solid lines. Since more than a degree separates the Dark Field from individual W4 fields, it can be assumed that sky profiles will always be an approximation of the nearby night-sky emission to be subtracted. Induced by a less than perfect subtraction of the λ6553.6 OH line and the λ6562.8 geocoronal Hα line[1], small remnants are detected near the right wing of different Hα profiles in (the faintest) Fields 21, 22, and 23 (see, in particular, the lower panels in Figures 3, 4, and 5). The fact that these remnants show important variations on the FOV suggests that the night-sky emission varies on angular distances of less than 12′ on the plane of the sky. Gaussian fits were also applied on these remnants (not shown in Figures 3–5 to avoid unnecessary complexity). The reader is, however, referred to the residuals of the fits symbolized by the small black dots in Figures 3–9. The base line (continuum) at zero was also traced out to help estimate the relative importance of the residuals. Finally, the vertical and horizontal thick solid lines are respectively associated with the centroid position and the observed line width of each fitted Hα profile. In order to extract purely kinematic broadening effects from the observed line widths, the method of quadratic subtraction presented in Paper I was again used. For every panel, the LSR radial velocity, $v_{i,\mathrm{LSR}}$, the corrected line width value, $\beta_{i,\mathrm{corr}}$, and the S/N of the fitted line are given. For Figures 3–9, error bars on $v_{i,\mathrm{LSR}}$ and $\beta_{i,\mathrm{corr}}$ correspond to kinematic uncertainties and are derived from the method introduced by Lenz & Ayres (1992).

Table 1 presents a review of the kinematic information extracted from Fields 21 to 27. For each field, the mean LSR radial velocity and mean corrected line width are given respectively in Columns 3 and 4. From now on, the label "i" will be referring to the field's identification number (e.g., $\langle v_{21,\mathrm{LSR}} \rangle$ corresponds to the mean radial velocity observed in Field 21). The number of cycles (M) accumulated for both the Dark and W4 fields (see Figure 2) is presented in Column 5. Exposure times for each W4 field can be estimated at $7 \times$ M minutes. This time does not take into account the time spent on DF (for a given W4 field, the total time of telescope required to obtain a reliable kinematics is, therefore, estimated at $7 \times 2 \times$ M minutes). Column 6 gives the angular separation (between optical centers) between each W4 field and the Dark Field. Finally, a brief comment on the particular location of each field is provided in Column 7. The value for $\langle \beta_{22,\mathrm{corr}} \rangle$ was treated as an upper limit due to particular Hα profiles (see Panels (c), (h), (j), and (l) in Figure 4) that revealed undefined (numerically) $\beta_{i,\mathrm{corr}}$ values (see Section 4.1 in Paper I). Kinematically, these profiles were interpreted as being extremely narrow with line widths below 1 km s^{-1}, but were ignored in the calculation of the mean corrected line width of Field 22 (see Section 5.3). Uncertainties, in Columns 3 and 4, correspond to kinematic uncertainties obtained from the mean Hα profile associated with each field.

In the following section, we compare the kinematics of each field to see if there may be flows between fields. Relevant characteristics are presented in Table 2 for those fields in our Hα survey of W4-north which are probably connected in this way. The linear radial velocity and line width gradients are presented respectively in Columns 2 and 3. In Column 4, the range corresponds to the distance on the plane of the sky separating the two connected fields. The gradients were calculated using

[1] The top abscissa, in Figures 3–9, corresponds to the scanned wavelength interval of the FPI's central interference order. Paper I mentioned a spectral scanning that covers seven interference orders for a 60 Å range (roughly seven times the free spectral range on rest Hα). Each order wraps around the others and is summed on each channel at the end of the acquisition. A given channel, therefore, corresponds to more than one wavelength. However, the central interference order dominates the flux at roughly every step except at the particular spectral positions of the contaminant night-sky lines. Peripherical orders do not account for the detected spectra, flattened out by the narrow-band filters.

Table 1
LSR Radial Velocity and Line Width Investigations

Field	Optical center (l,b)	$\langle v_{i,\mathrm{LSR}}\rangle$ (km s^{-1})	$\langle \beta_{i,\mathrm{corr}}\rangle$ (km s^{-1})	M	Separation (°)	Location
21	(134.°45, 6.°35)	-59.3 ± 0.5	8.6 ± 0.8	22	1.°21	Top-cap break
22	(134.°00, 6.°50)	-68.7 ± 0.8	<3.7[a]	28	1.°54	Top-cap break
23	(133.°85, 4.°75)	-51.5 ± 0.7	9.3 ± 1.3	26	1.°05	Top-cap break
24	(132.°60, 4.°40)	-33.1 ± 0.3	10.0 ± 0.6	28	2.°34	Western-side break
25	(133.°65, 3.°55)	-38.9 ± 0.3	13.6 ± 0.6	20	2.°01	Horizontal sheets
26	(135.°65, 4.°60)	-37.7 ± 0.6	17.0 ± 0.7	18	1.°04	Eastern shell
27	(135.°40, 3.°80)	-38.4 ± 0.2	18.2 ± 0.3	18	1.°46	Eastern shell
DF	(134.°80, 5.°20)	N/A	N/A	N/A	N/A	Dark Field

Notes. For Fields 21–23, panels labeled "No Fit" were not considered in the calculation of $\langle v_{i,\mathrm{LSR}}\rangle$ and $\langle \beta_{i,\mathrm{corr}}\rangle$.
[a] An upper limit is found due to Hα line widths estimated below 1 km s^{-1}. These particular panels were not statistically considered in the calculation of $\langle \beta_{22,\mathrm{corr}}\rangle$.

mean values in Columns 3 and 4 of Table 1. Of course, we assume the flow to be continuous between the fields. Table 2 is mainly relevant to the verification of our model of a pierced metal container discussed in Section 5.2.

5. DISCUSSION

5.1. Motivation

To determine whether or not ionized material is escaping the H II region through the fragmented shell, a large-scale investigation of the ionized gas's kinematics of W4-north is necessary. A particular kinematic signature, directed from the center of the superbubble toward the breaks, should be observed if indeed ionized material flows beyond the boundaries of W4 (see Section 1). A large-scale trend in radial velocities is immediately deduced from Table 1. On a "south-to-north" direction, apparently directed toward the top-cap break (see Figure 1), radial velocities change approximately from -40 km s^{-1} (in Fields 25 and 27) to -70 km s^{-1} (in Field 22). In particular, values measured for $\langle v_{21,\mathrm{LSR}}\rangle$ and $\langle v_{22,\mathrm{LSR}}\rangle$ are clearly blueshifted with respect to the H I supershell (see Section 2). We believe that the kinematic behavior of the embedded material in W4-north resembles the behavior predicted by pressurized air in a metal container suddenly pierced along its wall. A simple model of this rarefaction scenario is derived in Section 5.2, which allows us to obtain the velocity of the rarefied material expanding toward the wall opening. In our interpretation of our Hα survey, particular attention will be given to the ionized material found in the vicinity of the possible top-cap (see Section 5.3) and western-side breaks (see Section 5.4).

5.2. Analogy: W4-North as a Pierced Metal Container

We previously presented our intuition that a shell opening associated with W4-north could eventually be modeled by a rarefaction wave propagating inside a pierced metal container (see Sections 1 and 2). Figure 13 foreshadows the model suggested by our analysis (see Sections 5.3–5.6). To simplify the description, we will assume (for now) that only the shell's polar cap has been proned to fracture. The rarefaction wave is bordered, in Figure 13 by the two weak discontinuities moving in opposite directions (see Section 5.8); Discontinuity-N is moving toward the galactic corona and Discontinuity-S toward the galactic mid-plane. Discontinuity-N is labeled by a question mark since no kinematic information is provided by our Hα survey above Field 22. This field, still showing evidence for an accelerated ionized component (see Table 1), indicates that Discontinuity-N can be located somewhere above $b \sim 6.°5$ (see Section 5.7). The location of Discontinuity-S in Figure 13 is investigated in detail in the discussion to follow.

We follow Landau & Lifshitz (1987), who present textbook examples of semi-infinite cylindrical pipes in which rarefaction waves dominate the kinematics of the embedded gaseous material. The particle density and pressure of any gas element within a pipe decrease as the wave moves. This basically defines rarefaction. Rearranging the authors' Equation (99.15), we obtain the relation for the velocity v_ρ of the gaseous material behind (above) Discontinuity-S with respect to the gas said at rest located in front of (below) it:

$$v_\rho = \frac{2c_0}{(\gamma - 1)} \times \left[1 - \left(\frac{\rho}{\rho_0}\right)^{\frac{\gamma-1}{2}}\right], \quad (1)$$

where c_0 is the speed of sound in the vicinity of the gas at rest, γ is the heat capacity ratio of the accelerated material, and ρ_0 is the particle density of the gas at rest. The variable ρ is the local particle density of the rarefied material. For W4, the speed of sound was estimated at 10 km s^{-1}. The heat capacity ratio of a monoatomic ideal gas, neutral or ionized, is 5/3. However, the lack of energetic photons at high-galactic latitudes (Terebey et al. 2003; Dennison et al. 1997; West 2003) suggests that the plasma in W4-north can be interpreted as a mixture of perfect gases still undergoing ionization (this can be seen, in particular, from a thin H I supershell above $b = 4°$ and the presence of the H I horizontal sheets). The heat capacity ratio's equation for atomic hydrogen is provided by Cox & Giuli (1968) and is shown in Figure 10 for an ionization rate between 0 and 1. A portion of the curve is isolated for an ionization rate between 0.95 and 0.99, a range of values we consider plausible for W4-north. The heat capacity ratio is, therefore, estimated between 1.10 and 1.30.

From Equation (1), a family of curves is traced out in Figure 11 for five different values of γ (1.10, 1.15, 1.20, 1.25, and 1.30). The relations show the expected behavior in velocities as the gaseous material is rarefied (toward Discontinuity-N) following the passing of Discontinuity-S (see Figure 13). Since the value for ρ/ρ_0 diminishes as the material moves away from Discontinuity-S, a relation is likely to exist between a particular gas element's particle density and the distance it has traveled inside the rarefaction wave (i.e., between the two discontinuities). The abscissa in Figure 11 is, therefore, an indicative of the distance (increasing from right to left) separating the accelerated material and the discontinuity moving

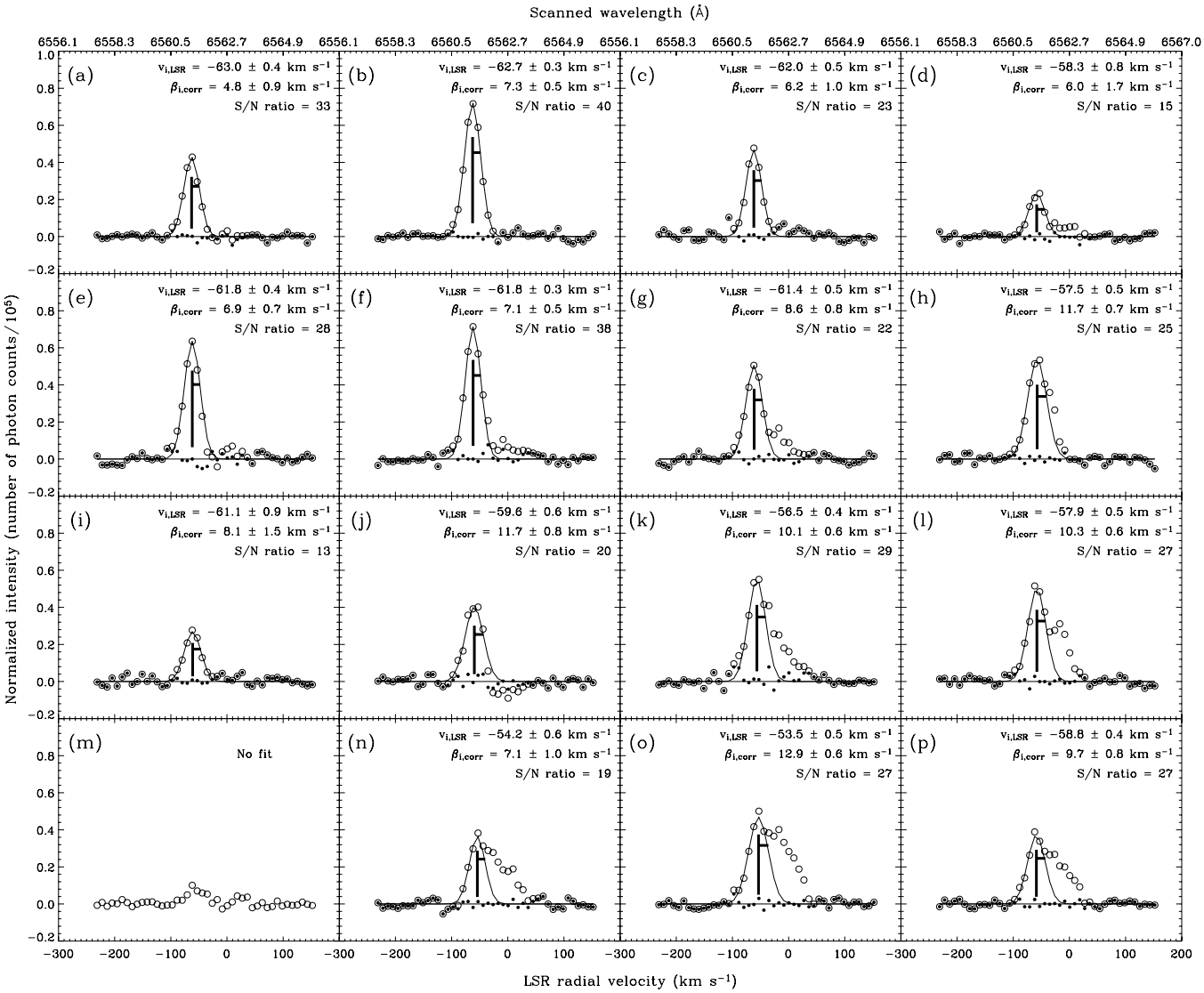

Figure 3. Hard binned Hα profiles for Field 21.

into the gas at rest. The velocity gradient remains constant until the ratio ρ/ρ_0 reaches approximately 10%. Over the same range, the variations of γ do not seem to have sizeable repercussions on the kinematic behavior (this remains true for roughly any value of γ below 1.50). Below 10%, however, the velocity gradient becomes much steeper and presents a larger dispersion with the heat capacity ratio since the $(\gamma - 1)^{-1}$ term dominates the exponent in Equation (1). In every case, the peak velocity is found at $2c_0/(\gamma - 1)$ when the rarefied material becomes so tenuous that its local particle density can be interpreted as 0 with respect to the density of the gas at rest ($\rho/\rho_0 \rightarrow 0$). For the analogy of a pierced metal container, this corresponds to the maximal velocity at which the embedded pressurized air can be ejected through the opening (using, obviously, the correct values for c_0 and γ).

The model presented here is unidimensional and would be appropriate if we suppose chimneys to form in a roughly cylindrical shape. In this case, only a corrective term, required from the fact that we measure radial velocities and, therefore, taking into account the angle of inclination of the "cylinder" with respect to the observer, would need to be applied to the curves in Figure 11. However, the W4 region, in particular, brings some geometrical constraints. For example, the apparent size of the top-cap break is much smaller ($\sim$10%) than the maximal width of the large superbubble (West et al. 2007). We, therefore, assume the zone of rarefaction, between the two discontinuities in Figure 13, to resemble the shape of an inverse light bulb. Our model might, therefore, be proned to uncertainties as we investigate at ionized material located more and more away from a central vertical axis passing by $l \sim 134\overset{\circ}{.}2$. Moreover, a probable western-side break (see Section 5.4) would certainly induce a rather complicated kinematics in W4-north since the embedded ionized material would be dominated by two rarefaction waves instead of one. All of these reasons demand a three-dimensional model to be eventually derived.

Our one-dimensional model also does not provide indications for the behavior in line widths as the ionized material travels away from the discontinuity moving into the gas at rest. First, we must consider the fact that the gas at rest, in W4, probably presents a kinematics in agreement with what we referred to as the "chaotic" interflow medium in Paper I. From its location close to the center of the W4 superbubble, this component likely present a large diversity of radial velocity gradients along the line of sight (a large volume of embedded ionized

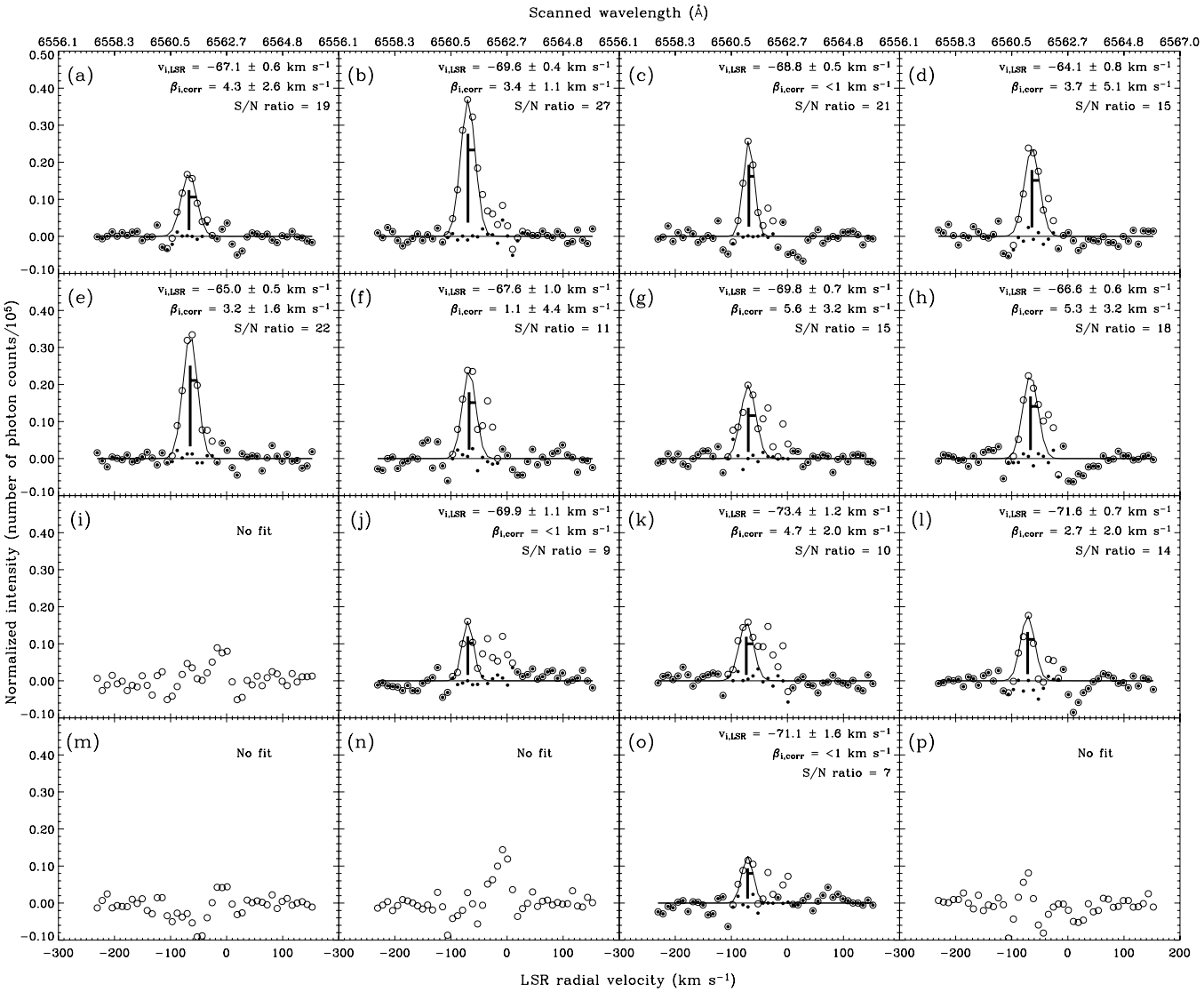

Figure 4. Hard binned Hα profiles for Field 22.

material being investigated). Moreover, freshly ionized material is constantly provided resulting from the photoionization of the atomic shell. The sustainment in gas likely contributes to turbulence in the interflow medium. These arguments are all related to the large Hα profiles observed in Paper I. Intuitively, we can anticipate line widths will decrease above the southern discontinuity in Figure 13 for two reasons. First, the production of turbulence being suppressed following the passing of a rarefaction wave (Gol'dfel'd et al. 1987), we expect a monotonic dissipation of the vorticity as the material travels away from the southern discontinuity. Secondly, the fact that the rarefied material converges straight at the shell opening diminishes the number of radial velocity gradients along the line of sight in the zone of rarefaction. Our assumptions, therefore, propose the ionized material found above Discontinuity-S to generally appear more and more "ordered" with latitude. For our Hα survey, this would result in a narrowing of the observed line widths with spatial change (from Discontinuity-S to -N). This line narrowing gradient (see the definition used in Section 4.1 of Paper I) should, therefore, be correlated with the large-scale radial velocity gradient expected from Figure 11.

5.3. Top-Cap Break

Gathered in the vicinity of the H I-spur filament (Normandeau 2000), Fields 21 and 22 coincide with the northernmost latitudes investigated in our Hα survey. We reiterate the fact that this particular region of W4 appears as a closed shell lining in Hα images but also reveals a fracture according to the atomic observations (see Section 2), therefore, pinpointing a possible top-cap break in a very low density H I shell. From Figure 1, Fields 21 and 22 are located slightly above the hypothetical H I fracture. At this height above the star cluster IC 1805, the ionized material is extremely tenuous (Dennison et al. 1997). This can be seen from Figures 3 and 4 where the extraction of reliable information has not been possible for particularly faint areas labeled "No Fit." We assume the faint Hα emission detected in both fields to be associated with the polarized data (tracing the superbubble) of West et al. (2007) rather than, say, foreground objects.

Examination of Table 1 shows that the northern Field 22 is more blueshifted, and has narrower lines, than the lower latitude Field 21. This can be interpreted as a "south-to-north" flow.

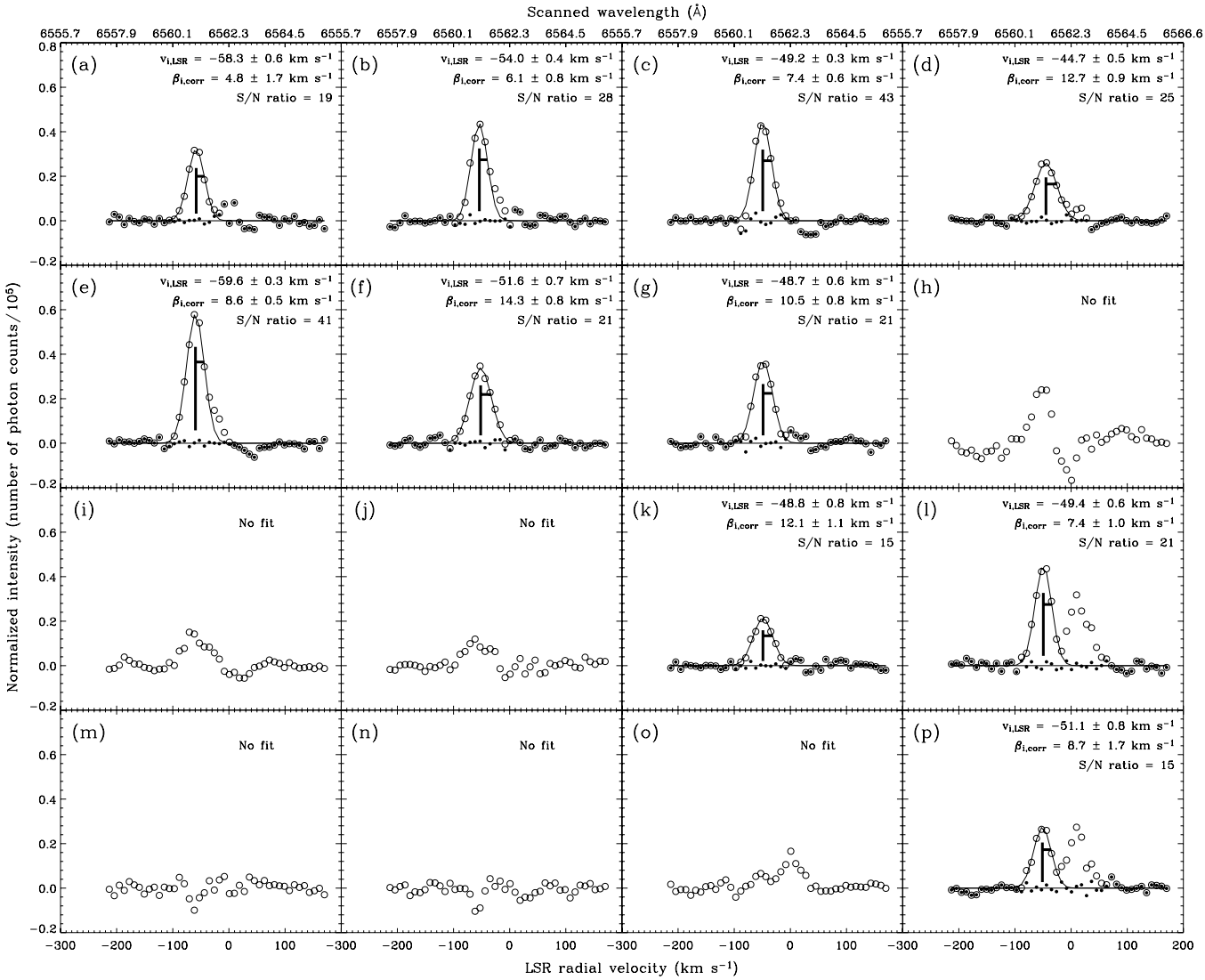

Figure 5. Hard binned Hα profiles for Field 23.

The fact that $\langle v_{21,\mathrm{LSR}} \rangle$ and $\langle v_{22,\mathrm{LSR}} \rangle$ do not coincide with the radial velocity range of the H I supershell (see Sections 2 and 5.1) makes it difficult to associate the ionized gas with the shell. From our model presented in Section 5.2, the orientation indicated by the line narrowing gradient should be correlated with the direction of the ionized flow itself. From the slight tilt toward the observer expected from the W4 superbubble (Normandeau et al. 1996; Lagrois & Joncas 2008) and the well-defined blueshifted radial velocity gradient directed toward the galactic corona, we propose the observed behavior to correspond precisely with the signature anticipated from the passing of a rarefying discontinuity, the rarefaction wave itself being induced by the appearance of an opening near the shell's polar cap.

In Figure 3, the "south-to-north" tendency toward line narrowing is also well-defined intrinsically in Field 21. From a roughly sonic regime in Panels (j) to (l), northern edge's line widths present values slightly above 6 km s^{-1}. The "south-to-north" blueshifted radial velocity gradient is also easily detected within Field 21 in agreement with the tendency presented on a larger scale in Table 1. Particularly visible along the two middle columns from Panels (n) and (o) to (b) and (c) respectively, the kinematic trend leads to northern radial velocities slightly more negative than -60 km s^{-1}.

On an intermediate scale, estimated at roughly 19 pc between Fields 21 and 22, the radial velocity and line width gradients are found respectively at $\nabla_v = (-)0.49$ km s^{-1} pc^{-1} and $\nabla_\beta = (-)0.26$ km s^{-1} pc^{-1} (see Table 2). The larger (in absolute value) radial velocities obtained from our Hα survey are found in Figure 4 where lower panels show radial velocities slightly below -70 km s^{-1}, blueshifted by nearly 25 km s^{-1} with respect to the neutral expanding supershell. The Hα line widths also show a clear continuity from Field 21 to 22 as the highly accelerated ionized material evacuates the W4 superbubble, aiming toward the galactic corona. In fact, four panels in Figure 4 present Hα profiles so narrow that the spectral resolution of our interferometric device system does not allow us to properly resolve the width of the fitted lines. Hence, either (1) the kinematic disorder (including turbulence) is minimal along the line of sight (see Section 5.7), (2) the electron temperature is smaller than the canonical value (7400 K) used so far in this work, or (3) all of the above. A good estimate of the electron temperature is critical in order to convert observed line widths in

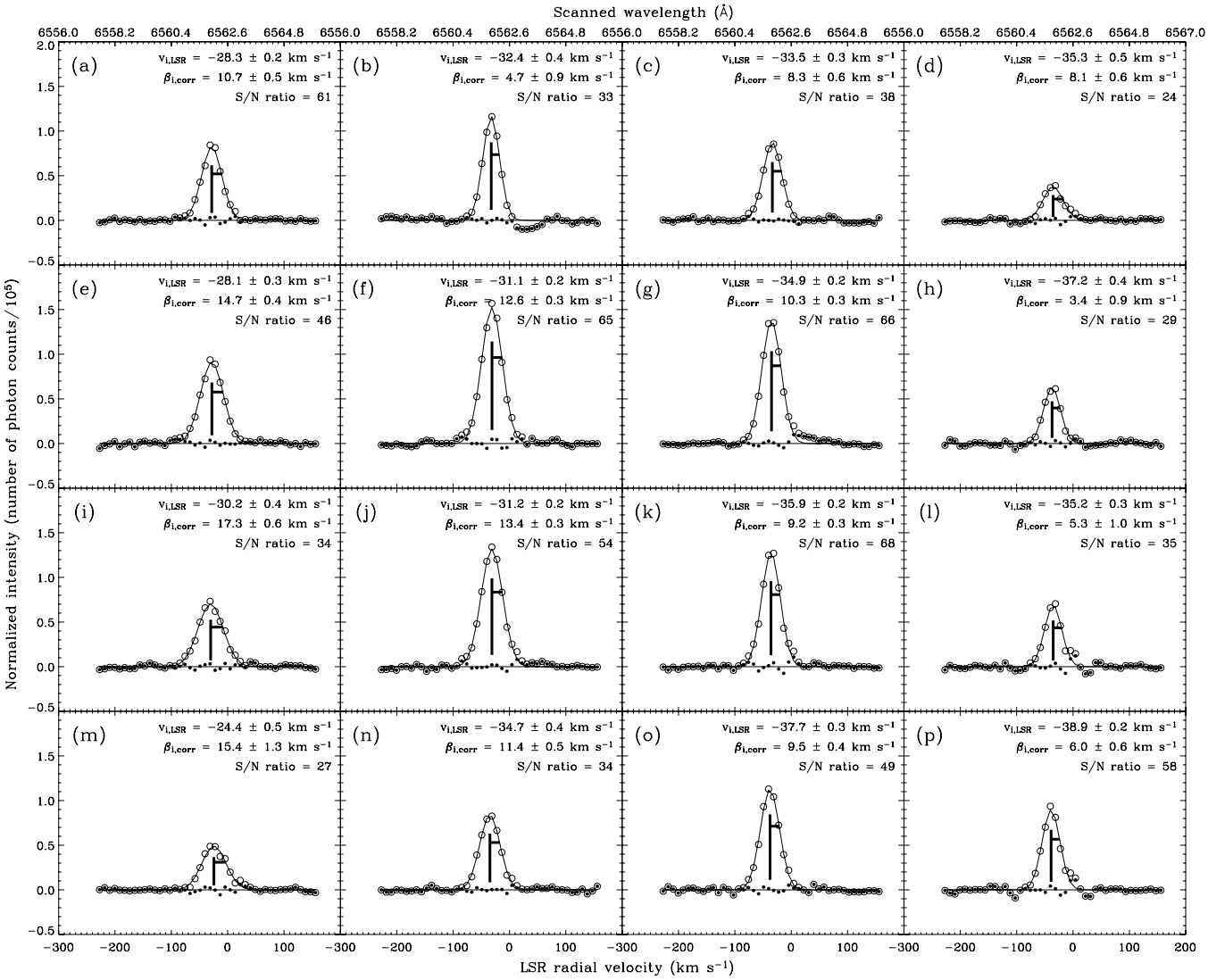

Figure 6. Hard binned Hα profiles for Field 24.

purely kinematic line widths (see Section 3 in Paper I). Certainly, a slight overestimation of the electron temperature[2] in W4-north is plausible if we assume a large fraction of the most energetic photons (of the star cluster IC 1805) to be absorbed by neutral material embedded in W4-south (see Paper I). The overestimation will lead (numerically) to line widths narrower than it should be. However, the fact that the abundance of neutral material in W4-north is relatively small (see Section 5.2), we can argue that the electron temperature is probably constant in W4-north and does not decrease with latitude. Therefore, the line narrowing gradient pointing toward the galactic corona is genuine. On the other hand, the overestimation of the thermal broadening likely contributes to undefined $\beta_{i,\mathrm{corr}}$ values ($<$1 km s^{-1}) in Field 22.

From our investigation of Fields 21 and 22, it is reasonable to assume that a discontinuity associated with a rarefaction wave had previously accelerated and forced the ejection of ionized material beyond the boundaries of the W4 superbubble. In order to estimate the distance over which this discontinuity, traveling toward southern latitudes, has affected the embedded ionized material, Field 23 was observed. The field resides halfway between the northern polar cap and the possible western-side break (West et al. 2007). A particularly weak signal is observed near its south-east boundary. Six panels in Figure 5 have failed to show well-defined profiles mainly due to a slight overlap with the Hα-poor cavity observed in the middle of W4-north (see Figure 1). In agreement with Fields 21 and 22, Figure 5 shows a clear tendency toward line narrowing from the middle Panels (f), (g), and (k) to the north-east boundary in Panels (a), (b), and (e). The line width gradient is precisely oriented toward the top-cap break. The anticipated blueshifted radial velocity gradient is also observed as northern radial velocities are found barely more positive than -60 km s^{-1}, slightly redfshifted with respect to the radial velocities in the northern portion of Field 21. This is however in agreement with Field 23 being located closer to the southern discontinuity than Field 21 and, therefore, presenting a kinematics slightly more in agreement with what we expect from the gas at rest (see Figure 11). From the values obtained in Table 1 for $\langle v_{21,\mathrm{LSR}} \rangle$ and $\langle v_{23,\mathrm{LSR}} \rangle$, we calculated a particularly flat radial velocity gradient estimated at $\nabla_v = (-)0.11$ km s^{-1} pc^{-1} in Table 2. The gradient is however likely limited (in steepness)

[2] The lower limit for the electron temperature of the galactic diffuse ionized medium (hereafter, DIM) has been estimated to 5400 K from forbidden line intensities (Reynolds 1989b).

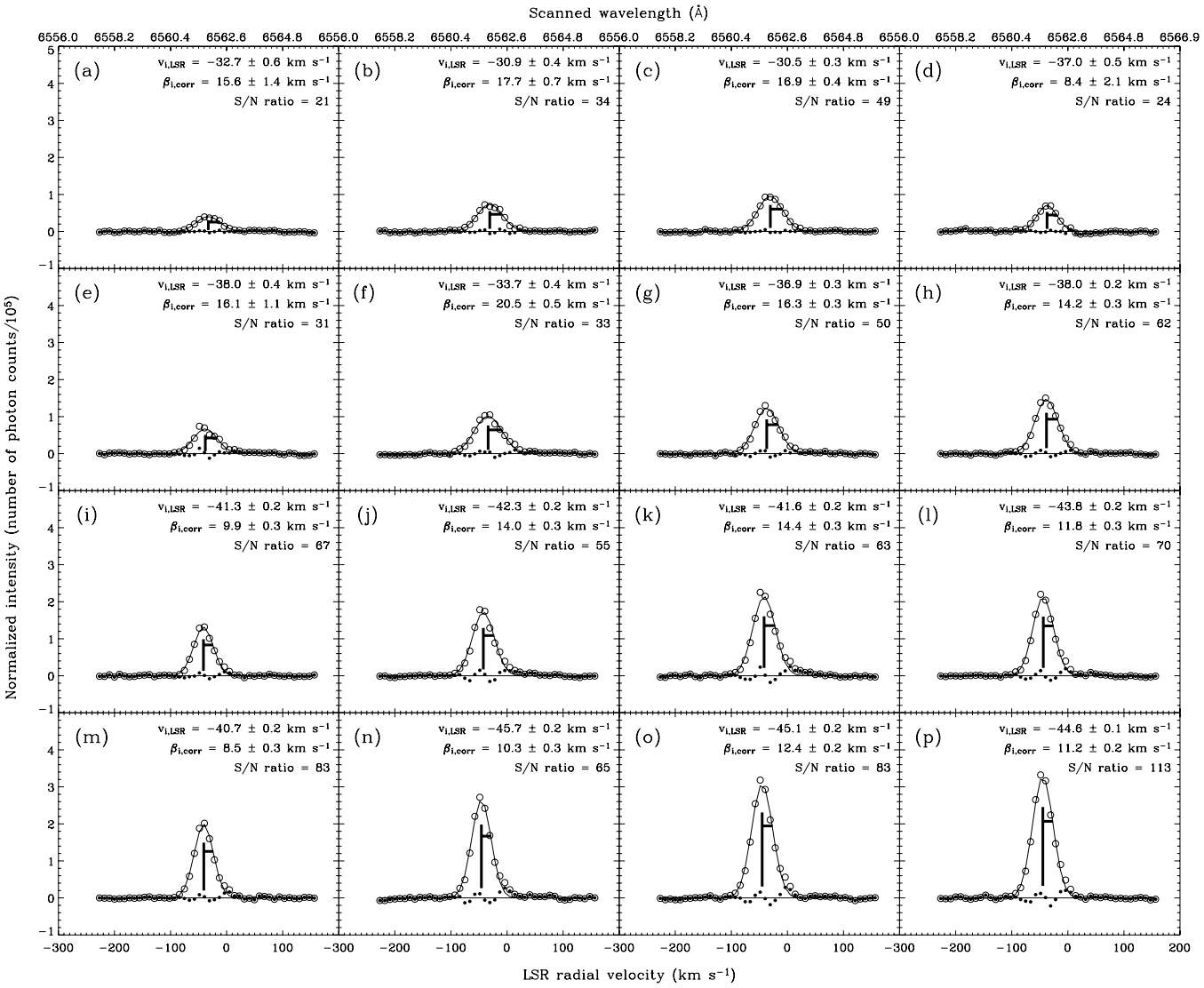

Figure 7. Hard binned Hα profiles for Field 25.

from the fact that it is measured on a more or less oblique axis (see Section 5.7). Moreover, considering the W4 superbubble to be only slightly tilted toward the observer (an argument used in Paper I to explain the low kinematic disorder on the plane of the sky), relatively flat radial velocity gradients are not surprising in W4-north. Hence, our model presented in Section 5.2 essentially uses kinematic observations in order to describe a scenario of outward gas venting occurring over a particularly extended range, rather than associated with a very steep gradient.

A well-defined signature in the northern portion of W4-north allowed us to confirm striking similarities between our model of a rarefaction scenario and the kinematics of Fields 21 to 23. A kinematic impact on the embedded ionized material has been observed on a range estimated at 72 pc between Fields 22 and 23 and was attributed to a rarefying discontinuity associated with the top-cap break and propagating toward the galactic mid-plane. An investigation on a larger scale will however be provided in Section 5.7. We will also compare, in Section 5.8, the rate of escape of the ionized material through the chimney with respect to the filling rate in W4-north (provided by the inner erosion of the atomic shell). The fact that the polar cap, in particular, has been proned to shell instabilities (and, therefore, fracture) is not surprising since a low particle density is expected from upstream ISM material more and more tenuous with the increasing galactic latitude. A low electron density is directly correlated with a low recombination rate of the ionized shell (Dyson & Williams 1980). Numerical simulations have shown the amplitude of developing instabilities to enter a growth regime when recombination processes are turned off or highly diminished (Mizuta et al. 2005). The kinematic confirmation of a top-cap break is of great importance as it clearly indicates that the W4 superbubble is currently evolving into a chimney. Considering the remarkable alignment (toward the galactic corona) taken by the top-cap break, escaping photons (through the hole) will undoubtedly contribute to the sustainment of the high-latitude Reynolds loop (Reynolds et al. 2001).

5.4. Western-Side Break

The investigation of the second breakout identified by West et al. (2007) is provided by Field 24. A brief review should however be made on Field 23. We already demonstrated its upper half to enclose ionized material kinematically in agreement with the presence of a top-cap break (see Section 5.3). On the other

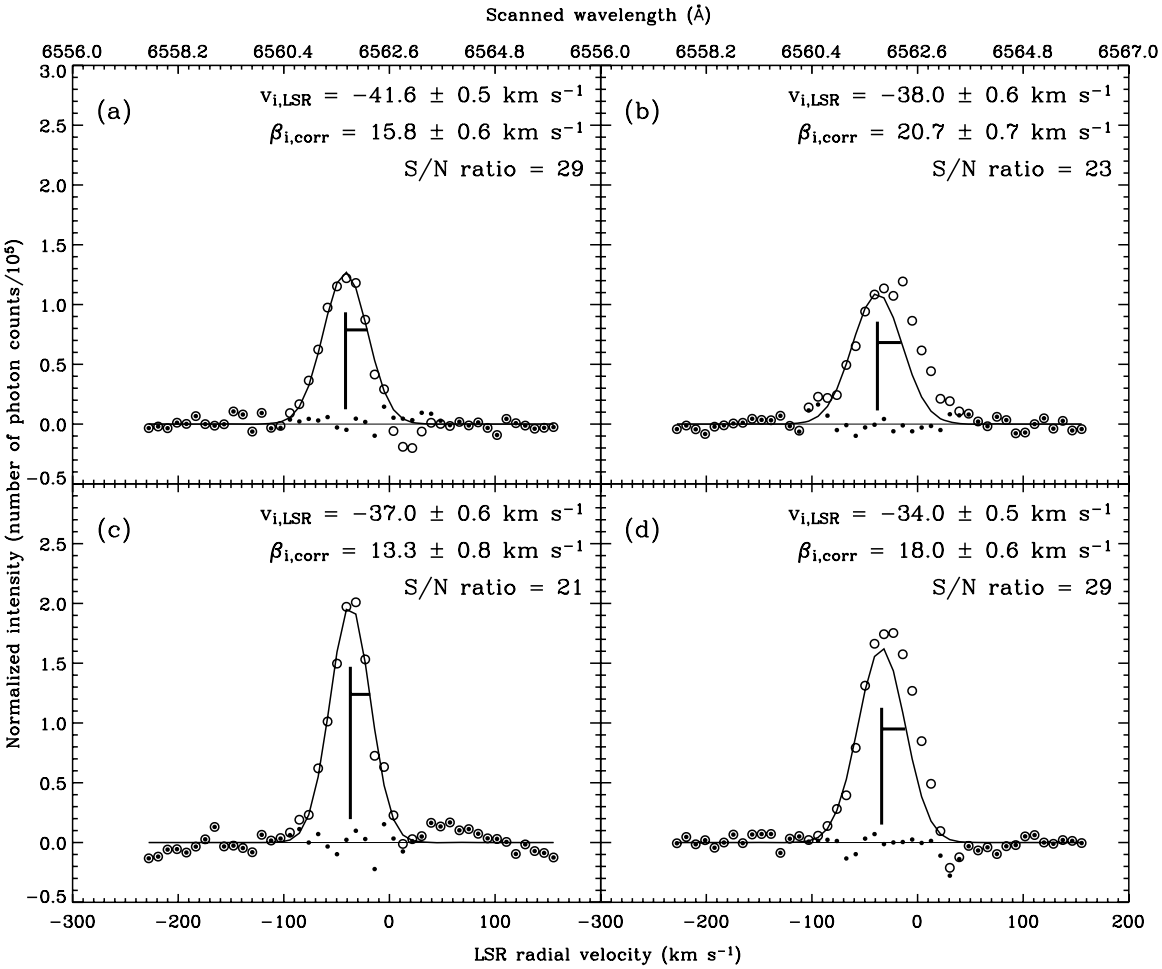

Figure 8. Hard binned Hα profiles for Field 26.

hand, a second gradient toward line narrowing is possible, from the middle to the lower panels in Figure 5, oriented toward the western-side break. However, Figure 6 (for Field 24) does not favor any connection with Field 23 as its eastern boundary shows supersonic line widths. From our model (see Section 5.2), we would expect a significant decrease in line widths from the lower panels in Figure 5 to the easternmost panels in Figure 6 as the ionized flows converge toward the western-side break.

Certainly, we anticipate the embedded material in W4-north to be kinematically dominated by two possible regimes: the erosion of the embedded atomic material (H I walls and horizontal sheets) or the large-scale trend expected from rarefaction waves. The former possibility was largely discussed in Section 5.3 of Paper I in which we suggest the eroded material to lag behind the advancing (toward the observer) bubble. This is similar to the wake of material behind a solid body moving in a viscous fluid. The resulting kinematics is likely to show an ionized component redshifted with respect to the H I supershell. This is what was found for Fields 04, 17, and 18 in Paper I. However, the radial velocities approaching −50 km s^{-1}, in Panels (k), (l), and (p) of Figure 5, do not coincide with this scenario. Even though a possible implication of the western-side break near $b = 5^\circ$ has been ruled out by the disconnection in line widths between Fields 23 and 24, the kinematics of Field 23 seems to be entirely attributed to the passing of a rarefying discontinuity propagating toward southern latitudes. We, therefore, assume that the kinematic repercussions attributed to the top-cap break can be found on a distance that likely exceeds the 72 pc range previously estimated (see Section 5.5).

On the other hand, the investigation of Field 24 provides inconclusive results for the presence of a western-side break. Certainly, the blueshifted radial velocity gradient combined with a line narrowing gradient (both being precisely oriented toward the western wall) represent a signature identical to the kinematic behavior observed in Field 21. However, radial velocities between −30 and −40 km s^{-1} do not present a significant discrepancy with the radial velocity range of the H I supershell. In fact, interpreting Figure 6 along a "west-to-east" direction, the kinematic behavior appears very similar to what we would expect from the erosion of atomic material. The radial velocity gradient presents a redshifted tendency estimated between 1.1 and 2.3 km s^{-1} pc^{-1} (these are respectively the flatter and steeper gradients measured from the four rows in Figure 6), perfectly matching our results for Flows D, T, and U in Paper I. A line broadening gradient is found slightly below 2 km s^{-1} pc^{-1}, also coinciding with Flow D. However, the investigation of the CGPS H I observations clearly indicates that the shell is ill-defined in the vicinity of Field 24 (Normandeau et al. 1997). This argument alone favors the large side break detected by West et al. (2007) while the striking similarities established between Field 24 and Fields 04, 17, and 18 are likely coincidental.

Two reasons are proposed to explain why the kinematics of Field 24 does not indicate the presence of a shell opening along the western wall of W4. First, if the outflows are oriented

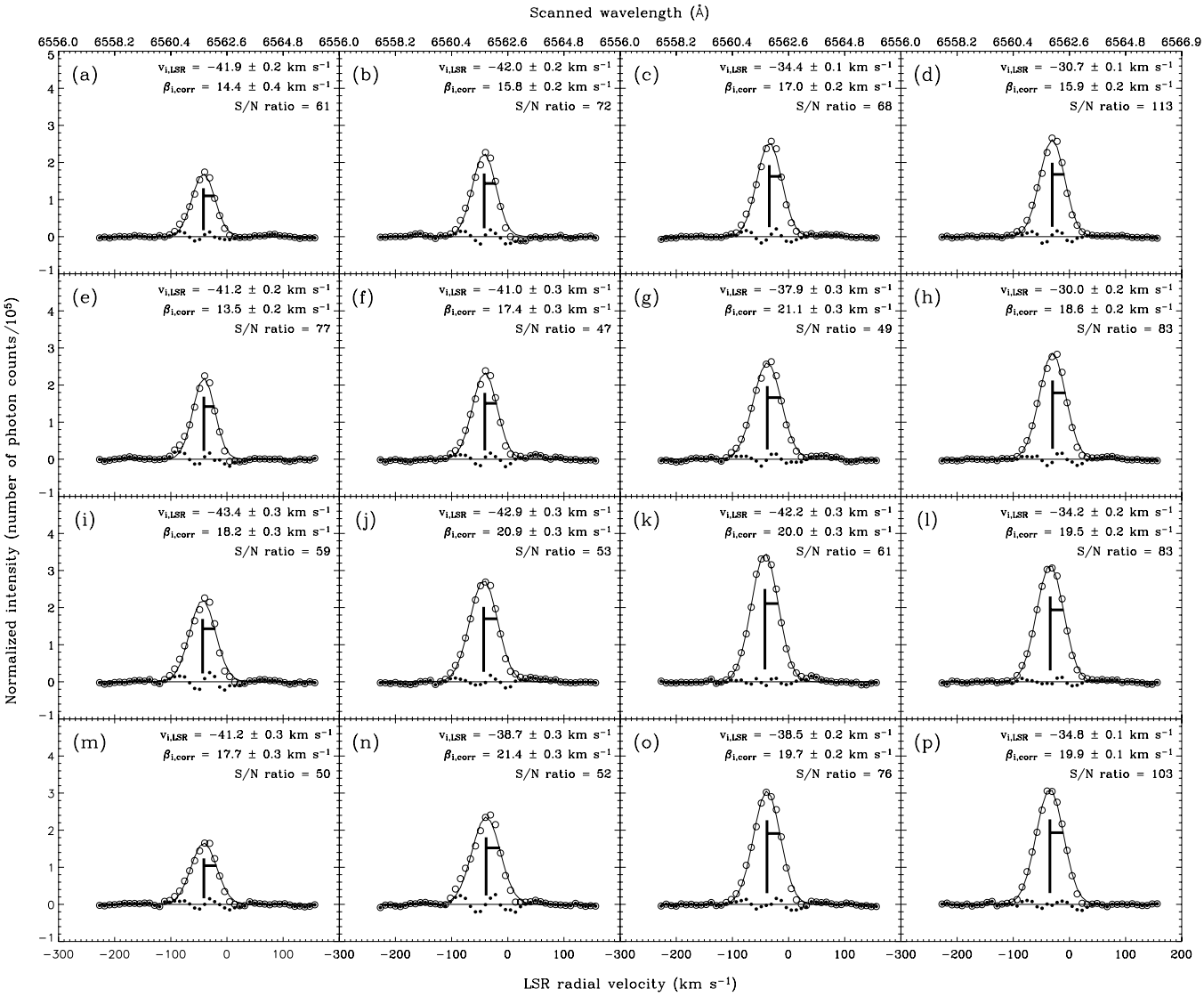

Figure 9. Hard binned Hα profiles for Field 27.

roughly perpendicular to the line of sight (in other words, if the outflows do not "follow" the tilt of the superbubble as we would expect), this particular geometry would artificially maintain the radial velocities roughly in agreement with the gas at rest. The important discrepancy in radial velocities between the ionized material and the H I supershell (see Section 5.3) would remain undetected. Secondly, it can be assumed that the western-side break is relatively young or, at least, much younger than the top-cap break. We can reiterate the fact that the development of shell instabilities in an expanding superbubble is supposed to initially occur near the shell's polar cap (Dove et al. 2000). In this case, it is reasonable to assume that the rarefaction near Field 24 would still be very low (that is, to assume a ρ/ρ_0 value, introduced for Figure 11, very close to 1). This assumption, we believe, supercedes the first one; not only does it explain radial velocities almost in agreement with the atomic shell but it is also in agreement with the "east-to-west" gradients (in radial velocities and line widths) observed in Field 24. We, therefore, propose a scenario in which a discontinuity, probably located not too far away from the field's eastern boundary, travels toward larger longitudes. In order to further investigate on a possible western-side break, a western extension to Field 24 is required (e.g., the dashed line "empty field" on the right of Field 24 in Figure 1). This extension would certainly enclosed ionized material more rarefied (than in Field 24) and, therefore, radial velocities slightly more different than the atomic shell.

Similar to the top-cap break, the implication of a western-side break is also important from the point of view of the dynamical evolution of the expanding wind-blown bubble (see Section 5.8). However, its hypothetical orientation, favoring evacuated flows of ionized material roughly parallel to the galactic mid-plane, would not allow for an efficient connection with the galactic corona. On the other hand, the escaping photons would certainly contribute to the photoionization and sustainment of the DIM found at low-galactic latitudes (Mathis 1986).

5.5. Horizontal Sheets

The H I horizontal sheets mark the boundary between the emissive more W4-south region and the much fainter W4-north. The spectroscopic 21 cm line observations of the CGPS revealed the horizontal sheets on a LSR radial velocity range between -38 and -45 km s^{-1} (Normandeau et al. 1997). Roughly located at the geometrical center of the expanding superbubble,

Table 2
Linear Kinematic Connections Between Individual Fields

Fields	∇_v (km s^{-1} pc^{-1})	∇_β (km s^{-1} pc^{-1})	Range (pc)
21 → 22	(−)0.49	<(−)0.26[a]	19
23 → 21	(−)0.11	(−)0.01	70
25 → 23	(−)0.24	(−)0.09	49

Notes. Arrows in Column 1 should be translated as "From the Field XX to Field YY."

[a] The line width gradient was calculated using $\langle\beta_{22,\mathrm{corr}}\rangle = 3.7$ km s^{-1} and is, therefore, likely to be slightly steeper than presented. The "<" symbol signifies that the gradient can only be more negative.

Field 25 investigates the kinematic behavior of the tenuous ionized material found below the Hα-poor cavity (see Figure 1).

Similar to Field 23, the north-east portion of Field 25 is (spatially) close to the imposing dark region almost fully deprived of Hα emission. In Figure 7, this leads to weaker Hα profiles in Panels (a), (b), and (e). Radial velocities approaching -45 km s^{-1} can be found in Panels (n) to (p), slightly blueshifted with respect to the horizontal sheets; the neutral features are particularly well-defined at this specific location with radial velocities between -41 and -42 km s^{-1} (Normandeau et al. 1997). From the four columns in Figure 7, a "south-to-north" radial velocity gradient, directed toward the top-cap break, is estimated to be between 1.2 and 2.3 km s^{-1} pc^{-1}. The gradient is redshifted (with respect to the southern panels in

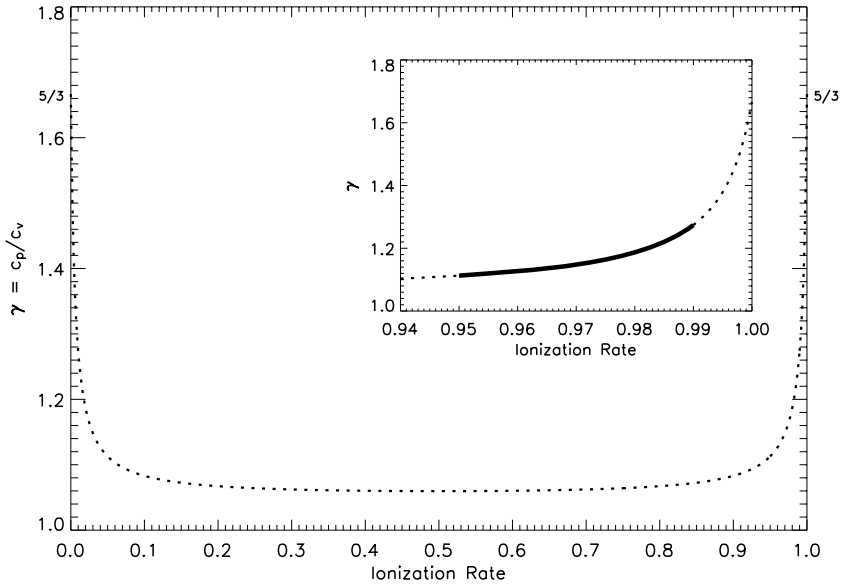

Figure 10. Heat capacity ratio for monoatomic hydrogen undergoing ionization. The dotted curve is obtained from Equation (9.169) of Cox & Giuli (1968) assuming an electron temperature of 7400 K. The magnified curve (solid line) isolates the heat capacity ratio for an ionization rate between 0.95 and 0.99.

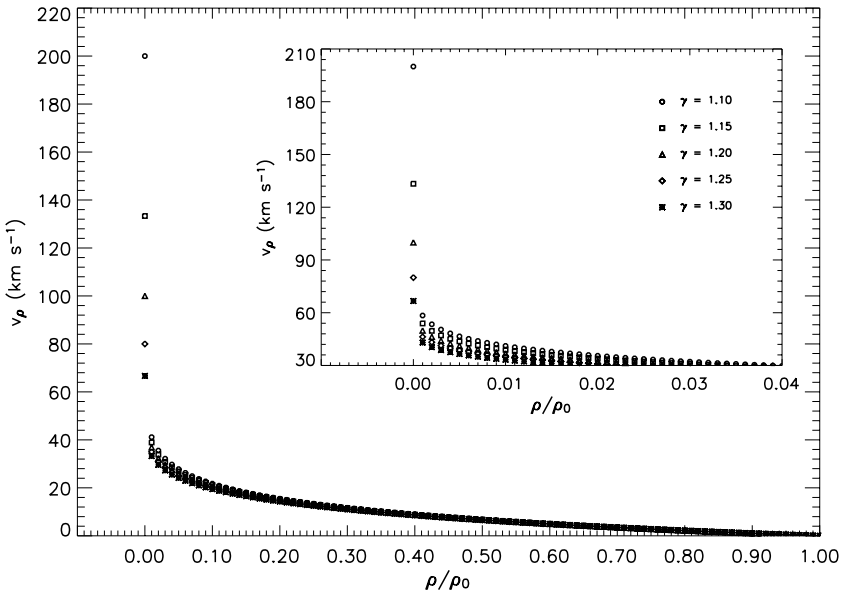

Figure 11. Behavior in velocities expected in a rarefaction wave likely associated with W4-north. Equation (1) was plotted using $c_0 = 10$ km s^{-1}. The velocity v_ρ of the rarefied material (measured with respect to the gas at rest) is traced out w.r.t. ρ/ρ_0. The variable ρ indicates the local particle density of the rarefied material while ρ_0 indicates the particle density of the gas at rest. Discontinuity-S is located at $\rho/\rho_0 = 1$ and Discontinuity-N, at $\rho/\rho_0 = 0$ (see Figure 13). The five curves correspond to different values of the heat capacity ratio: $\gamma = 1.10$ (open circles), 1.15 (open squares), 1.20 (open triangles), 1.25 (open diamonds), and 1.30 (stars). The magnified curves correspond to the possible solutions for W4-north.

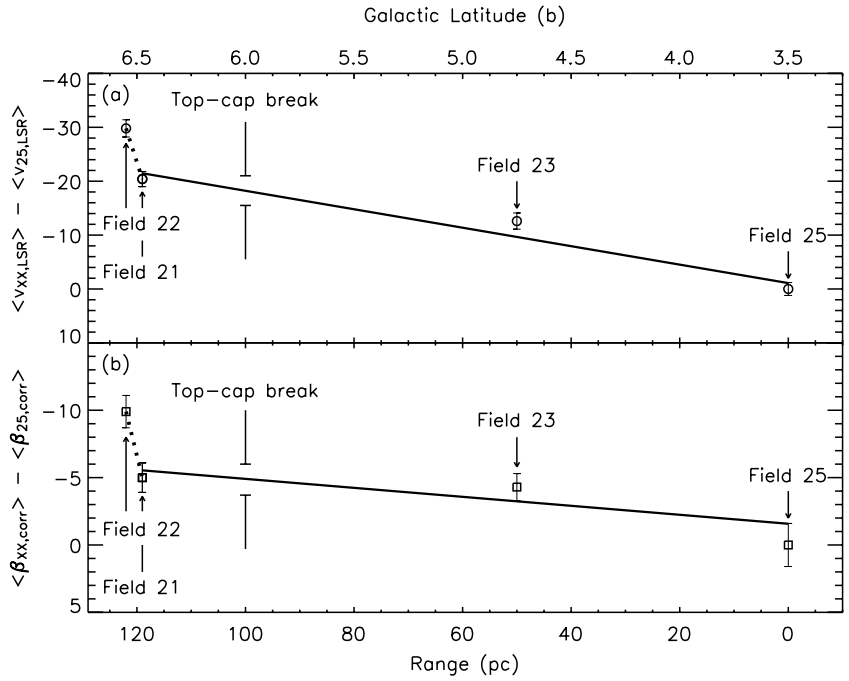

Figure 12. Large-scale (a) radial velocity, and (b) line width gradients in W4-north. The two ordinates are in units of km s^{-1}. Open circles and open squares correspond to the data points. On a range of 125 pc between Fields 25 and 22, each panel presents two trends. The kinematic connections between Fields 25, 23, and 21 show radial velocity and line width gradients (solid lines) estimated at $\nabla_v = (-)0.17 \pm 0.04$ km s^{-1} pc^{-1} and $\nabla_\beta = (-)0.04 \pm 0.02$ km s^{-1} pc^{-1} respectively. The Pearson correlation coefficents applied to the straight lines are found to be -0.97 and -0.85 respectively. The kinematic connections between Fields 21 and 22 show radial velocity and line width gradients (dotted lines) estimated at $\nabla_v = (-)3.13$ km s^{-1} pc^{-1} and $\nabla_\beta < (-)1.63$ km s^{-1} pc^{-1} respectively. The inequality for ∇_β comes from the fact that we used $\langle\beta_{22,\mathrm{corr}}\rangle = 3.7$ km s^{-1}, the upper limit on the mean line width of Field 22. In other words, the line narrowing gradient can only be more negative than $(-)1.63$ km s^{-1} pc^{-1}. The top abscissa gives approximately the galactic latitude for each field. At $b = 6°$, the position of the top-cap break is indicated in both panels.

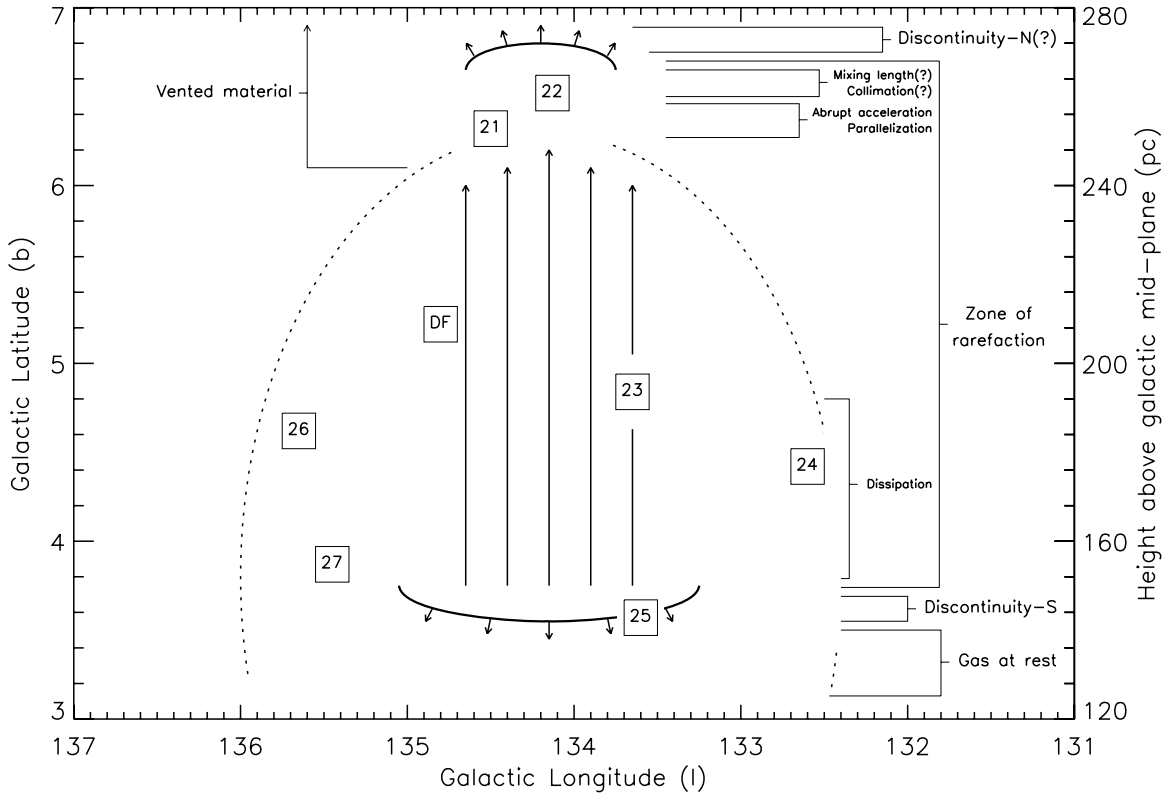

Figure 13. Application to W4-north of our model of a pierced metal container governed by the propagation of a rarefaction wave. The different regions (gas at rest, discontinuities, zone of rarefaction) are traced out following our kinematic analysis of Fields 21–27 in Sections 5.3–5.7 (see the text). Small arrows indicate the direction of motion associated with the two discontinuities enclosing the rarefaction wave. Long arrows show the direction of motion of the rarefied material between the two discontinuities. The threshold $b = 6°$ marks the latitude above which the ionized material has been vented beyond the boundaries of the H II region, above the top-cap break.

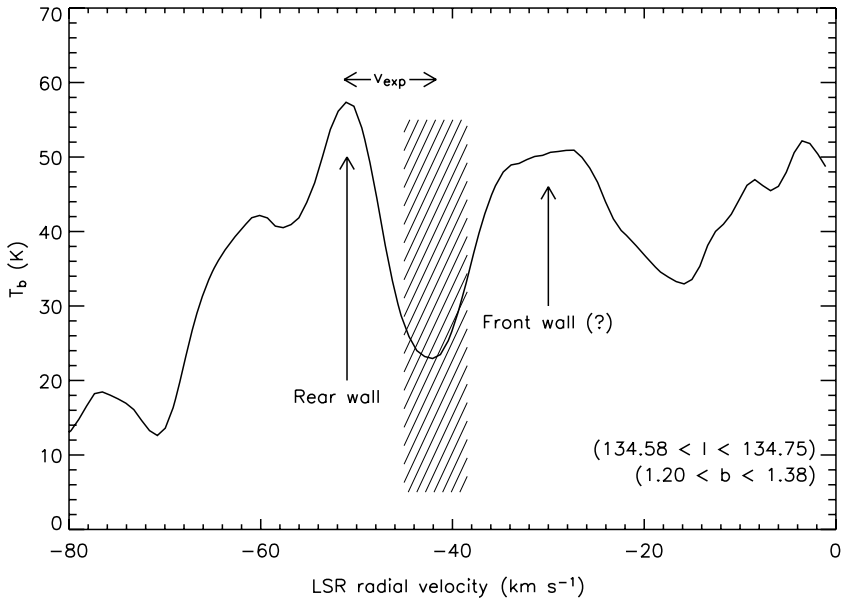

Figure 14. Radial velocity profile extracted from the CGPS 21 cm line observations along the line of sight of W4-south. The rear wall of W4 is clearly detected from the well-defined peak near −51.3 km s^{-1}. The front wall peak, much broader, is likely to be contaminated by a large-scale neutral feature located between the expanding bubble and the observer. The dashed area shows the radial velocity range associated with the H I cavity revealing the W4 H II region. The actual expansion velocity of W4 is estimated at 9.75 km s^{-1} from the radial velocity range between the H I cavity and the position of the rear wall.

Figure 7) and, therefore, cannot be related to the same dynamical process described for Fields 21 and 22 (see Section 5.3). On the other hand, the gradient's steepness perfectly matches the radial velocity gradients observed for Flows D, T, and U in Paper I. In fact, the kinematics of Field 25 is almost identical to what was found for Fields 04, 17, and 18; the ionized material, eroded from the horizontal sheets, could be observed in the wake of the advancing (toward the observer) neutral filaments. This supposes the horizontal sheets to be located in front of the star cluster, tilted in a way that their southern edge is slightly in front of their northern edge (from a side point of view). Assuming this scenario, the lagging material would certainly be in agreement with the redshifted radial velocity gradient.

Disregarding the western column from Panel (p) to (d), a line broadening gradient, pointing away from the atomic material, is estimated at 0.8 km s^{-1} pc^{-1} in Figure 7. The gradient is much flatter than 2.1 km s^{-1} pc^{-1}, the value measured for ∇_β in Flow D (see Table 4 in Paper I). However, the steepness coincides very well with the line width gradients estimated for Flows T and U (see Table 4 in Paper I). The discrepancy in line widths between Flow D and Flows T and U was explained by much more tenuous atomic material in Fields 17 and 18 when compared to Field 04 (see Section 5.3 in Paper I). Larger line widths can be partially related to the accumulation of different radial velocity gradients along the line of sight and this scenario is highly favored in presence of dense erodible material. If we assume the particle density of the horizontal sheets to roughly equal the one of the W4 eastern shell near Fields 17 and 18, it could explain the line width behavior in Field 25. The fact that $\langle\beta_{25,\mathrm{corr}}\rangle$ (see Table 1) is well into the supersonic regime, and roughly in agreement with $\langle\beta_{\mathrm{interflow,corr}}\rangle$ (see Figure 4 in Paper I), could indicate a kinematics also partially explained by the interflow medium (see Section 5.7). This is expected since the location of Field 25 allows for deep lines of sight through the W4 superbubble (see Section 5.2).

However, the proximity of Field 25 to the Hα-poor cavity (see Figure 1) may also be a factor that explains the relatively flat "south-to-north" line broadening gradient in Figure 7. In Section 5.3, the kinematics of Fields 21, 22, and 23 were presented as being directly related to the passing of a rarefying discontinuity propagating toward the galactic mid-plane and associated with an opening near the shell's polar cap. If we assume that Discontinuity-S has reached the vicinity of Field 25 (see Figure 13), the Hα-poor cavity in Figure 1 could be filled of accelerated ionized material (flowing toward the top-cap break), rarefied to such a degree that it becomes roughly invisible (see Section 5.7). The ionized component of Field 25 could, therefore, be the most recently material "incorporated" into the evacuation process (in Figure 11, this corresponds to material found at $\rho/\rho_0 = 1$).

The transition (from unperturbed to accelerated and rarefied material) could initially be characterized by a localized attenuation of the line broadening gradient (expected from the erosion of the H I material) before becoming the line narrowing trend observed on a larger scale (see the kinematic connections between Fields 23 and 21 and Fields 21 and 22 in Table 2). If this attenuation takes place on a range of a few parsecs on the plane of the sky, the line width gradient's flatness in Field 24 might correspond to it. However, a northern extension of Field 25, at the periphery of the Hα-poor cavity (e.g., the dashed line "empty field" above Field 25 in Figure 1), would be required in order to precisely detect the kinematic signature anticipated from a rarefaction wave. The kinematic connection between Field 25 and Field 23 is presented in Table 2. A factor of two is measured between the radial velocity gradient connecting Fields 25 and 23 and the one connecting Fields 23 and 21. Again, this is due to the particularly oblique connection linking the two latter fields (see Sections 5.3 and 5.7). On the other hand, the line narrowing gradient between $\langle\beta_{25,\mathrm{corr}}\rangle$ and $\langle\beta_{23,\mathrm{corr}}\rangle$, nine times steeper than for Fields 23 to 21, is probably associated with more than just a geometrical effect (see Section 5.7).

The investigation of Field 25 proposes the southern discontinuity (associated with the polar cap's rarefaction wave) not to have traveled below the threshold fixed by the H I horizontal

sheets. Even though the particular kinematic signature expected from our model in Section 5.2 could not be explicitly identified near $b = 3.^{\circ}5$, we anticipate the southernmost signs of gas venting outwards to appear slightly below the Hα-poor cavity. This would give a range of roughly 125 pc separating the southern discontinuity and Field 22 slightly above the top-cap break's vicinity (see Section 5.7).

5.6. High-Latitude Eastern Wall

The investigation of the W4 eastern wall at high galactic latitude ($b > 3^{\circ}$) is provided by Fields 26 and 27. Non-photometric sky conditions, absorbing high-altitude cirrostratus, and a lack of accumulated cycles have constrained us to spatially degrade the raw data cube of Field 26 to obtain 2×2 images. Even though the statistics are poor (only four points being available in Figure 8), the detected motion of the ionized material is nonetheless in agreement with the kinematic behavior observed in Fields 04, 17, and 18 (see Paper I). From the inner erosion of the eastern wall, lagging material seems to flow toward the center of the wind-blown bubble. On an "east-to-west" direction, the redshifted radial velocity gradient is estimated as slightly below 1.1 km s^{-1} pc^{-1}. From the location of Field 26, roughly 5 to 8 pc separates it from the eastern wall. Extrapolating the radial velocity gradient leads to radial velocities roughly in agreement with the 21 cm line observations showing the neutral shell with velocities between -43 and -46 km s^{-1} (Normandeau et al. 1997). In Figure 8, the expected "east-to-west" line broadening gradient is found at 1.2 km s^{-1} pc^{-1}, a steepness that coincides with an intermediate case scenario between Flow D and Flows T and U. Eastern line widths in Panels (a) and (c), well above 10 km s^{-1}, also clearly indicate a gradient "in progress" since a transition from a subsonic to a supersonic regime is expected from the inner erosion of the neutral wall (see Section 5.3 in Paper I). Extrapolating the line width gradient for the missing range between Field 26 and the compressed shell leads to line widths between 4 and 8 km s^{-1} in agreement with dispersion values associated with the shell material in Fields 04, 17, and 18 (see Paper I).

Similar to Field 26, Field 27 is characterized by a redshifted radial velocity gradient again directed away from the neutral wall toward the Hα-poor cavity and is estimated to be just below 1.5 km s^{-1} pc^{-1} in Figure 9. A 30 pc interval separates the optical center of Field 27 from the nearby eastern shell. Extrapolation, on this range, of the radial velocity gradient leads to radial velocities more negative than -80 km s^{-1}, obviously in disagreement with the 21 cm line observations (Normandeau et al. 1997). The inner erosion of the eastern wall does not properly explain the kinematic behavior of Field 27. Table 1 presents a slightly blueshifted value for $\langle v_{27,\mathrm{LSR}} \rangle$ when compared to $\langle v_{26,\mathrm{LSR}} \rangle$. Given a larger distance separating Field 27 from the neutral shell (than Field 26), we would expect a redshifted tendency between mean radial velocities from Field 26 to Field 27. The complicated kinematic behavior seen in Figure 9 could be related to a contribution of radial velocities more negative than -38 km s^{-1}. This blueshifted material (with respect to $\langle v_{27,\mathrm{LSR}} \rangle$) is likely to be associated with the photoerosion of the H I horizontal sheets. At the longitude of Field 27, the neutral filaments present radial velocities just below -45 km s^{-1}, slightly blueshifted from the H I material found in the vicinity of Field 25 (Normandeau et al. 1997). Criss-crossing ionized flows resulting from the proximity of two distinct erodible features (the filaments and the H I wall segment) could explain the accumulation of different gradients along the line of sight of Field 27. This would also explain the value for $\langle \beta_{27,\mathrm{corr}} \rangle$, about 20 km s^{-1} which is the largest observed in both W4-south and -north.

5.7. A Large Scale Trend in W4-North

The investigation of the ionized material in W4-north (see Sections 5.3–5.6) implies there are kinematic connections, in radial velocities and line widths, between four of our Hα fields (see Table 2). Figure 12 provides, on a vertical scale of roughly 125 pc, the large-scale trends of W4-north. Field 25 (see Table 1) coincides with the kinematics of the gas at rest near the southern discontinuity caused by the top-cap break's rarefaction wave. Every radial velocity and line width point in Figure 12 is measured with respect to $\langle v_{25,\mathrm{LSR}} \rangle$ and $\langle \beta_{25,\mathrm{corr}} \rangle$, respectively. This can be justified from the fact that Field 25 displays mean values of radial velocity and line width in agreement with $\langle v_{\mathrm{interflow,LSR}} \rangle$ and $\langle \beta_{\mathrm{interflow,corr}} \rangle$ for the interflow medium (see Section 5.5). The interflow medium was introduced, for W4-south, as ionized material not a priori associated with a well-identified or well-defined Champagne flow (see Paper I). These areas seem to be partially formed of material that results from the inner photoerosion of the H I supershell. In Paper I, we supposed this interflow medium to account for a large fraction of the embedded ionized material in W4 and, therefore, likely constitute the medium in which the weak discontinuity propagates (toward the galactic mid-plane). The abscissa in Figure 12 corresponds to the distance on the plane of the sky separating each field from Field 25. Each panel shows two particular trends: relatively flat radial velocity ($\nabla_v = (-)0.17$ km s^{-1} pc^{-1}) and line width ($\nabla_\beta = (-)0.04$ km s^{-1} pc^{-1}) gradients between Fields 25, 23, and 21 while Fields 21 and 22 are spatially connected by much steeper relations ($\nabla_v = (-)3.13$ km s^{-1} pc^{-1}, $\nabla_\beta = (-)1.63$ km s^{-1} pc^{-1}). The gradients differ in steepness from Table 2 due to the fact that the connections were often made on a relatively oblique axis (e.g., 21 $\rightarrow$ 22, 23 $\rightarrow$ 21) rather than on a roughly vertical axis, the most plausible direction taken by the ionized outflows. Similarities can nonetheless be found between Figure 12 and Table 2 (in particular, the 21 $\rightarrow$ 22 connection showing the steeper gradients).

From the one-dimensional model of Landau & Lifshitz (1987), Equation (1) predicts a peak velocity of $v_{\rho,\max} = 2c_0/(\gamma - 1)$ for the rarefied material expanding behind Discontinuity-S (see Section 5.2). At this point (when $\rho/\rho_0 = 0$), the rarefied material overtakes Discontinuity-N to enter either a regime of constant velocity or a zone in which the velocity gradient quickly vanishes (see below, the last paragraph of this subsection). In Figure 12, no indications are provided for a break in the radial velocity gradient, which suggests that Discontinuity-N is undoubtedly located above or precisely at the location of Field 22, beyond the boundaries of the H II region. On the other hand, the sudden change of slope between Fields 21 and 22 resembles the kink in velocities predicted near $\rho/\rho_0 = 0.05$ in Figure 11 (this abrupt acceleration is indicated in Figure 13). The model, therefore, implies that the ionized material, initially swept-up by Discontinuity-S and presently ejected through the top-cap break, has been rarefied to at most 5% of the particle density of the ionized material near Field 25. In the vicinity of the shell opening, Field 22 shows a 30 km s^{-1} difference from the kinematics of the gas at rest in Field 25. Since we only measure radial velocities, the velocity jump between Fields 25 and 22 is undoubtedly larger. The section of our model showing velocity points larger than 30 km s^{-1}

is isolated in Figure 11. The "solution" for W4-north is likely found in these points. The large-scale blueshifted radial velocity gradient confirms the W4 superbubble to be tilted toward the observer, given the arguments in Section 5.3. The extremely small line widths near $b = 6.^{\circ}5$ (see Figure 4) indicate that the angle of inclination, with respect to the plane of the sky, is relatively small since Field 22 does not seem to probe the ionized material to a significant depth through the radial velocity gradient; otherwise, an important spreading in radial velocities would be anticipated along the line of sight. An estimation of its value can be made by assuming the 30 km s^{-1} difference to correspond to the peak (radial) velocity reached by the rarefied material (that is, to put Discontinuity-N in Figure 13 at the exact latitude of Field 22). Even though our survey cannot properly confirm the theoretical peak velocity to have been reached at the northernmost latitudes of W4-north, the kink detected between Fields 21 and 22 in Figure 12 could indicate that the vented material (see Figure 13) in the latter field presents a velocity near $v_{\rho,\max}$. If so, the inclination with respect to the plane of the sky is likely to be between 9° ($\gamma = 1.10$) and 27° ($\gamma = 1.30$).

The behavior in line widths is precisely in agreement with our expectations presented in Section 5.2. The much greater steepness characterizing the line narrowing gradient between Fields 25 and 23 when compared to the connection between Fields 23 and 21 (see Table 2) could be partially related to vortex dissipation immediately behind Discontinuity-S. In particular, supersonic turbulence will likely decay quickly once the material is incorporated inside the zone of rarefaction (Shu 1992). The zone of turbulence dissipation is indicated in Figure 13. From Table 1, values for $\langle\beta_{23,\mathrm{corr}}\rangle$ and $\langle\beta_{21,\mathrm{corr}}\rangle$ indicates a roughly constant trend in line widths between Fields 23 and 21. Even though we used a straight line to connect Fields 25, 23 and 21 in Panel (b) of Figure 12, one can immediately acknowledge roughly identical values, near −5 km s^{-1}, associated with the two latter fields. Above the zone of dissipation, we, therefore, assume the ionized material to be roughly deprived of turbulent motions; only a weak tendency related to the parallelization of the outflows could be responsible for the slight decrease in line widths (see below).

In Section 5.5, we interpreted the Hα-poor cavity (see Figure 1) as enclosing accelerated ionized material, rarefied by the passing of Discontinuity-S. The rarefaction is directed toward the top-cap break. From this assumption, the ionized material should appear more and more tenuous as the progression is made away from the weak discontinuity: that is, the rarefying discontinuity moves toward the horizontal sheets at $b = 3.^{\circ}5$ while the gas becomes more and more rarefied towards $b = 6.^{\circ}5$. According to our one-dimensional model, Field DF, used for sky subtraction (see Section 3), should, therefore, display an Hα emissivity greater than Fields 21 and 22 since it is located closer to Discontinuity-S and, therefore, should have a greater ρ/ρ_0 value (hence, less rarefied material). Field DF was used as a night-sky indicator due to the fact that it is located relatively far from the H I walls of W4-north. On the other hand, Field 21, in the vicinity of the shell's polar cap, might be constantly fed by freshly photoeroded material. The contribution of this material artificially accentuates the local particle density contrast, ρ/ρ_0. This allows a clear detection even at high galactic latitudes whereas the material in DF does not have sufficient contrast. However, the kinematics predicted by the model remain unchanged as the newly ionized component immediately acquires the high velocities of the nearby rarefied material. In Figure 3, there is no evidence for radial velocities near −45 km s^{-1}, a value locally associated with the H I wall.

Located relatively far (roughly 20 pc) from the H I shell (similarly to Field DF), the contribution in material mentioned in the previous paragraph cannot explain the "high" Hα emissivity in Field 22. A possible scenario can however be deduced if we make a few assumptions regarding the geometry of the ionized flows beyond the top-cap break. In Section 5.2, we mentioned that the width of the top-cap break represents only a fraction of the superbubble's width. Intuitively, this should lead to well-parallelized outflows as the material evacuates the superbubble. That is, there will be fewer orientations of velocity vectors to contribute to the line of sight measurement, resulting in a steep line narrowing gradient between Fields 21 and 22 (see Table 2). If the outflows eventually collimate above the shell opening, this would lead to the accumulation of ionized material in a small, restricted region above the top-cap break and, therefore, a localized increase of the particle density. Due to this increase in density, the ionized material will be more emissive than expected in Field 22. The accumulation of material directly favors the development of turbulent motions. This scenario (of collimation leading to turbulence) seems however more significant in the northern portion of Field 22 (see Panels (g) and (h) of Figure 4 with line widths slightly above 5 km s^{-1}) while the lower panels show a minimal kinematic disorder along the line of sight (see Section 5.3). Although an increase in density due to collimation causes line broadening, this could possibly be compensated by the parallelization of the outflows (which likely dominates the overall dynamics in Field 22 according to the small value found for $\langle\beta_{22,\mathrm{corr}}\rangle$ in Table 1).

Additionally, collimation could even lead to a slowdown of the vented outflows (see Panels (d), (e), and (h) in the northern portion of Figure 4 with radial velocities slightly more positive than $\langle v_{22,\mathrm{LSR}}\rangle$). This is deduced from the mass flow rate (i.e., the product of the particle density, the velocity, and the flow's cross sectional area) treated as being constant in Field 22. This is plausible since (from a previous argument) the field is located at a latitude above the eroded shell and, therefore, no ionized material is constantly added near $b = 6.^{\circ}5$. From the observed behavior in line widths, we already proposed in the previous paragraph that collimation becomes more and more significant with latitude inside Field 22. However, the fact that the particle density and the cross-sectional area of the outflows respectively increase and decrease on a "south-to-north" direction inside the FOV is not enough to definitively show that the velocities will also decrease. If the increase in density perfectly balances (numerically) the decrease in area, the velocities would remain unaffected by the collimating "bottleneck" effect. However, this possible deceleration of the outflows also favors (similarly to localized increase in particle density) the development of turbulent motions (Wang & Dalton 1991), again in agreement with larger line widths in the upper panels of Figure 4.

To the simplistic collimation model described above, a second dynamical scenario can also be considered in order to explain the kinematics observed in the northern portion of Field 22 (a kinematics, on a "south-to-north" direction, against the large-scale trends identified in Figure 12). From the formalism of Landau & Lifshitz (1987), the large-scale velocity gradient in Figure 12 is expected to vanish above Discontinuity-N (see Figure 13) if:

$$P_e < P_0 \times \left(\frac{2}{\gamma+1}\right)^{\frac{2\gamma}{\gamma-1}}, \qquad (2)$$

where γ is the heat capacity ratio of the accelerated material (see Figure 10), P_e is the external pressure to the superbubble, and P_0 is the pressure of the gas at rest embedded inside the

superbubble. Substituting our possible values for γ (between 1.10 and 1.30) and using the equation of state of a classical ideal gas leads (for the particular case of W4-north) to:

$$\frac{n_e}{n_0} \cdot \frac{T_e}{T_0} < 0.30\text{–}0.34. \quad (3)$$

We used canonical ratios of T_e/T_0 (0.01 to 0.1), between the cold, outer ISM and the warm, embedded material, and $n_e \sim 1$ cm^{-3} for the particle density of the atomic material found roughly 245 pc above mid-plane. The inequality of Equation (3) is not satisfied only if n_0, the density in the gas at the rest near Field 25, is $\lesssim$0.1 cm^{-3}. This value, which is well below the mean density of the galactic DIM (Mathis 1986), is unrealistic and hence we suppose that the rarefied material that overtakes the northern discontinuity dynamically evolves into the kinematic configuration of the local DIM beyond the boundaries of the large W4 H II region. This scenario is precisely identical to the concept of "mixing length" introduced in Paper I. Table 1 of Reynolds et al. (2001) gives the kinematic behavior of the DIM component located a few parsecs above Field 22; a mean radial velocity of roughly -45 km s^{-1} and a corrected line width of 16 km s^{-1}. Both the redshifted radial velocity and line broadening gradients observed from the two lower to two upper rows in Figure 4 could indicate material flowing above Discontinuity-N and mingling with the local DIM. This assumption contributes to put Discontinuity-N at a latitude of $b = 6\overset{\circ}{.}5$, coincident with Field 22. We firmly believe that this simple model of rarefied, vented material/DIM mixing supercedes the collimation scenario since it leads to an elegant connection with the data of the WHAM Northern Sky Survey.

5.8. The W4 Galactic Chimney: Suggestion of a Timescale Scenario

From our analysis of subsections Sections 5.3–5.7, we have strong evidence of a rarefaction scenario in W4-north which ultimately leads to gas venting outwards in the vicinity of the shell's polar cap. This corroborates the notion that a galactic chimney is currently forming inside the W4 superbubble. In the following subsection, a timescale scenario will be proposed in order to determine when W4 enters the chimney phase of its expansion; that is, to estimate at which time in the past the first signs of shell fragmentation would have been observed. Our model remains however approximate since it highly depends of the growth rate of the zone of rarefaction (see Figure 13) and, therefore, the velocity of the two weak discontinuities bounding the rarefaction wave. This information could only be roughly estimated from our observations. Finally, the rate of mass input associated with the photoerosion of the H I shell will be compared to the rate of escape of ionized material through the chimney.

Inconclusive results for a western-side break in Section 5.4 are of great importance (relative to the dynamical evolution of the W4 superbubble) as it implies the development of shell instabilities on a timescale much smaller than expected. This follows from our argument in Section 5.5 proposing that the large Hα-poor cavity (see Figure 1) formed by the evacuation of ionized material through the top-cap break alone. Dove et al. (2000) proposed the development of Rayleigh–Taylor instabilities that could lead to shell fragmentation once a supershell enters the re-acceleration phase of its expansion above the blowout threshold. We already demonstrated in Section 2 that W4 barely reaches the required height above the galactic mid-plane. However, three-dimensional models have shown that magnetohydrodynamic instabilities, in particular, are likely responsible for shell fragmentation at earlier stages (De Avillez & Breitschwerdt 2005; West et al. 2007). We expect the chimney to keep forming as long as the Hα-poor cavity does not occupy all the volume available inside W4 and the rarefaction wave does not dissipate.

From the kinematics observed in Fields 21, 22, 23, and 25, a simple time-dependent scenario, regarding the fragmentation of the shell's polar cap, can be derived. The fragmentation of the shell has necessarily occurred at a time when the shell's polar cap was located between 145 and 245 pc above the galactic mid-plane. The lower limit coincides with Field 25; otherwise, the Hα-poor cavity would be observed below the H I horizontal sheets and probably well into W4-south (see Section 5.5). The higher limit corresponds to the actual height reached by the egg-shaped supershell of West et al. (2007). The fragmentation of the shell coincides with the appearance of the two weak discontinuities associated with the rarefaction wave. The formalism of rarefaction waves (Landau & Lifshitz 1987) demands that the two discontinuities travel either along the same direction (toward the gas at rest) or in opposite directions. Since observational evidence suggests that Discontinuity-N is presently located above the W4 superbubble (see Section 5.7), this discontinuity is propagating toward the galactic corona. Otherwise, the discontinuity would be evident above Discontinuity-S in Figure 13 but still well below the actual height of the superbubble. The change of sign (from blueshifted to redshifted) of the large-scale radial velocity gradient, apparent in the northern portion of Field 22 (see Section 5.7), would, therefore, be observed at a latitude well below the top-cap break (which is not the case; see Figure 12). The fact that the two discontinuities are moving away from each other allows us to estimate the dynamical age of the zone of rarefaction.

Equation (4) of Dennison et al. (1997) defines the timescale t_D to be the time required for a superbubble to expand one scale height above the galactic mid-plane. Considering $H = 140$ pc above the galactic mid-plane (Normandeau 2000) and using the same values for the actual mechanical luminosity of the star cluster IC 1805 ($L_0 = 0.3 \times 10^{38}$ ergs s^{-1}) and the ambient particle density of the ISM exterior to the superbubble at the galactic plane level ($n_{\rm plane} = 5$ cm^{-3}), we obtain a new estimate of roughly 5.6 Myr for t_D, compared to 3.2 Myr proposed by Dennison et al. (1997). Assuming the superbubble to have expanded on a timescale between $1.5 \times t_D$ and $2.5 \times t_D$ (this type of approximation was also used by Dennison et al. (1997)) in order to reach its actual height (estimated at $1.85 \times$ H), we propose the dynamical age of the W4 superbubble to lay between 8.4 and 14.0 Myr. The lower limit is similar to the dynamical age of 9 Myr obtained by West et al. (2007).

The behavior in velocities of the two discontinuities associated with a rarefaction wave is particularly complicated as it involves viscosity and thermal conductivity in the gas at rest which ultimately lead to the dissipation of the wave in the subsonic regime (Landau & Lifshitz 1987). The velocities are however comparable to the speed of sound in the ambient plasma. If we assume both discontinuities to have a velocity of 15 km s^{-1}, the zone of rarefaction in Figure 13 is expected to have grown at a rate of 30 km s^{-1} (since the discontinuities are moving away from each other). Assuming Discontinuity-N to coincide precisely with Field 22 (an assumption largely discussed in Section 5.7), the point of shell fracture is estimated near $b = 5^\circ$ (halfway between $b = 3\overset{\circ}{.}5$ and $b = 6\overset{\circ}{.}5$), at a latitude coinci-

dent with Field 23 (roughly 200 pc above the mid-plane). For a distance of 2.35 kpc to the star cluster IC 1805 (Massey et al. 1995), this height corresponds to 1.4 × H, roughly 30% below the predicted blowout threshold (see Section 1). In order to cover, at a grown rate of 30 km s^{-1}, the distance of 125 pc between Fields 25 and 22, roughly 4.1 Myr is required. This can be interpreted as the dynamical age of the top-cap break and, consequently, the chimney. By subtracting the chimney's age from the range of dynamical ages obtained for the W4 superbubble (see above), shell instabilities are, therefore, likely to have developed 4.3 to 9.9 Myr following the ignition of the first stellar generation. As a check on this range of ages, we assume the mechanical luminosity to have remained constant (that is, near L_0) from one stellar generation to the other and we obtain, using Equation (1) of Mac Low & McCray (1988), the time required for a superbubble to reach a height of Z parsecs above the galactic mid-plane:

$$t(Z) = \left(\frac{Z}{1\ \mathrm{pc}}\right)^{\frac{5}{3}} \left(\frac{H}{1\ \mathrm{pc}}\right)^{-\frac{5}{3}} t_D. \quad (4)$$

For the W4 superbubble, roughly 10.1 Myr are necessary to reach 200 pc and initiate shell fragmentation. Adding the age derived for the chimney, our timescale scenario is in agreement with a dynamical age of 14 Myr for the superbubble, a value greater than the first estimate between 6.4 and 9.6 Myr proposed by Dennison et al. (1997). The authors, however, do not provide uncertainties on their estimate.

The velocity of 15 km s^{-1}, proposed in particular for Discontinuity-N, is probably not too far from reality. Our previous arguments have already demonstrated that Discontinuity-N, moving toward the galactic corona, is presently located slightly above the actual height of the superbubble, probably near the latitude of Field 22 (see Figure 13). In other words, the velocity of the discontinuity is probably slightly greater than the polar region's mean expansion velocity between 200 pc (at fracture) and 245 pc (actual height) above mid-plane. From Equation (13.5) of Lozinskaya (1992), giving the expansion velocity (with respect to time) of a wind-blown bubble in its phase of energy conservation, we predict a deceleration from 10.9 km s^{-1} (at Z = 200 pc and t = 10 Myr) to 9.6 km s^{-1} (at Z = 245 pc and t = 14 Myr). This is obtained using a mean particle density[3] of roughly 2 cm^{-3} for the upstream material between 37 pc (the height above mid-plane of the star cluster IC 1805) and 245 pc. For a mean expansion velocity of 10 km s^{-1}, the difference of 5 km s^{-1} between the region of the shell's polar cap and Discontinuity-N signifies that the weak discontinuity would have traveled an additional 20 pc during the last 4 Myr (corresponding to the age of the chimney). This simple argument puts Discontinuity-N at an height of 265 pc above the galactic mid-plane, in agreement with the location of Field 22 (see the right-hand axis of Figures 1 and 13).

Finally, an investigation is here provided that should help validate the relations established between our model of a rarefaction scenario and the kinematics of W4-north. The fact that the Hα-poor cavity is well-detected demands the rate at which the ionized material evacuates the superbubble to exceed the discharge (toward the interior) of freshly photoeroded material that results from the ionization of the neutral supershell. The rate $\dot{M}_{\mathrm{in}}$ at which the photoeroded material "falls" into the W4 superbubble is adapted (to our work) from the investigation of the photoevaporation of molecular clumps (Joncas & Roy 1984) and is estimated at:

$$\dot{M}_{\mathrm{in}} = \rho_{\mathrm{H\,II}}\, v_{\mathrm{H\,II}}\, S_{\mathrm{shell}}, \quad (5)$$

where $\rho_{\mathrm{H\,II}}$ correspond to the density (in units of mass per volume) of the ionized material in contact with the neutral shell, $v_{\mathrm{H\,II}}$ is the velocity of this material with respect to the neutral shell, and S_{shell}, the area covered by the shell. In order to avoid distortions of the velocity measurements due to a possible western-side break, we estimate $v_{\mathrm{H\,II}}$ to be roughly 1 km s^{-1} using Fields 04, 17, and 18 (Paper I, Table 5). The neutral supershell envelops an ionized superbubble. Thus using the characteristics determined by West et al. (2007), such as an half-radius and half-height of the W4 superbubble respectively of 82 and 123 pc, a particle density $\rho_{\mathrm{H\,II}}$ of ∼0.40 cm^{-3}, and noting that the zone of rarefaction covers about 30% of the superbubble area, we estimate $\dot{M}_{\mathrm{in}} \sim 3.4 \times 10^{-4}\ M_{\odot}\ \mathrm{yr}^{-1}$.

Using the same formalism as Equation (5), we obtained $\dot{M}_{\mathrm{out}}$, the rate of evacuation through the top-cap break, as

$$\dot{M}_{\mathrm{out}} = \rho_{\mathrm{break}}\, v_{\mathrm{evac}}\, S_{\mathrm{break}}, \quad (6)$$

where ρ_{break} is the density (in units of mass per volume) of the ionized material in the vicinity of the shell opening, v_{evac} is the velocity of the rarefied material passing above $b = 6°$, and S_{break}, the area of the top-cap break. We assume n_{break} (in units of particle per volume) to be roughly equivalent to the electron density, n_e, of Point I displayed in Table 4-2 and Figure 4-2 of West (2003). The value is estimated near 0.20 cm^{-3}. Using the large-scale radial velocity gradient of Figure 12 (solid line), we estimate the radial component of the velocity of evacuation (with respect to the gas at rest) to approximately 17 km s^{-1} at the position of the top-cap break ($b = 6°$). Using the range of values proposed for the superbubble's angle of inclination in Section 5.7, the velocity of evacuation v_{evac} is estimated between 37 km s^{-1} ($\theta = 27°$) and 110 km s^{-1} ($\theta = 9°$). West et al. (2007) gives 20 pc for the diameter of the top-cap break for a roughly circular shape of 315 pc^2. The value for $\dot{M}_{\mathrm{out}}$ is estimated between 5.9 × 10^{-5} and 1.8 × 10^{-4} $M_{\odot}$ yr^{-1}.

Our model of a W4 superbubble that looses ionized material at a rate faster than it gains material does not hold even for large values of v_{evac}. This could be explained by (1) a value for v_{evac} greater than expected (this would demand an ionization rate below 95% in W4-north leading to an angle of inclination with respect to the plane of the sky below 9°), (2) a sizeable contribution to the rarefied cavity attributed to the (young?) western-side break, (3) an underestimation of the break's dimensions, or (4) all of the above. For example, an angle of inclination slightly below 5° (instead of ⩾9°) or a shell opening characterized by a diameter of 28 pc (instead of 20 pc) would give $\dot{M}_{\mathrm{out}}$ greater than $\dot{M}_{\mathrm{in}}$, in agreement with our initial assumption. However, the increase in diameter (from 20 to 28 pc) would demand that the top-cap break, at the distance of W4, is more than 10 pixels wider than its current estimated width (according to the ∼1′ spatial resolution of the CGPS observations). Such a large difference with the CGPS images displayed in West et al. (2007) is highly questionable. A possible explanation might however be related to the shape of the top-cap break; rather than assuming a circular opening, an irregular,

[3] This value is justified by the exponentially decreasing galactic atmosphere model mentioned in Section 1. The atomic material displays a particle density of $n(Z) = n_{\mathrm{plane}} \times \mathrm{e}^{-Z/H}$. Assuming n_{plane} = 5 cm^{-3}, we obtain $\overline{n}$ = 2.01 cm^{-3} for Z varying between 37 and 245 pc. The CGPS 21 cm line observations (Normandeau et al. 1997) in W4-south exhibit an expansion velocity of 9.75 km s^{-1} for the W4 region (see Figure 14). Also, the W4-south region is used for the determination of the expansion velocity since both the front and rear walls of the supershell are ill-defined at the latitude of W4-north.

asymmetric break (that likely has a larger dimension along the line of sight compared to the dimension observed on the plane of the sky) could contribute for a larger $S_{\rm break}$ value. This is plausible since the edge-on view with the W4's polar cap does not allow to conclude on the shape of the shell opening.

6. CONCLUSION

The use of FaNTOmM, an interferometric device system especially designed to study particularly faint extended astronomical objects, has allowed us to extract the kinematic information associated with the ionized component found embedded in the northern portion of the galactic superbubble/H II region W4. Our motivation was based on the possible discovery that two faint H I segments along the northern shell could be interpreted as evidence of shell fragmentation (see Section 2). We propose a method of quantitatively identifying shell breakout (see Section 1). The method relies on the kinematic perturbation by (inward) propagating rarefaction waves. The results from using this method suggest a situation that is similar to a model of a pierced metal container (see Section 5.2).

A total of seven fields were observed in the galactic latitude range between 3° and 7°. Two kinematic regimes are identified. First, the embedded ionized material below $b = 5°$ and found at the periphery of the H II region seems to be mostly dominated by the inner erosion of the compressed H I shell (see Section 5.6), a behavior largely discussed in Paper I. However, a clear "south-to-north" gas flow is identified on a vertical axis of 125 pc between $b = 3.^{\circ}5$ and $b = 6.^{\circ}5$ (roughly centered on $l = 134°$), in agreement with the passing of a weak discontinuity (labeled Discontinuity-S in text) associated with a rarefaction wave (see Section 5.7). The discontinuity is propagating toward the galactic mid-plane and the rarefaction wave itself results from a shell opening near the polar cap. The second discontinuity of the wave (labeled Discontinuity-N in text) is propagating toward the galactic corona (see Section 5.8). Our investigation did not show conclusive results for ionized flows through a possible western-side break (see Section 5.4).

A 30 km s^{-1} radial velocity difference is found between Field 25 (which appears to be associated with the gas at rest near the southern discontinuity of the wave) and Field 22, enclosing the gas located slightly beyond the boundaries of the H II region (see Section 5.7). Between both these regions, a large Hα-poor cavity (see Figure 1) encloses accelerated and rarefied material expanding northward above (behind) Discontinuity-S (see Figure 13). Two trends in radial velocities are detected: a roughly flat gradient between Fields 25 and 21 estimated at $(-)0.17$ km s^{-1} pc^{-1} and a much steeper gradient found at $(-)3.13$ km s^{-1} pc^{-1} between the northern Fields 21 and 22 (see Figure 12). The sudden change of slope corresponds to the abrupt increase in velocities predicted from our model for highly rarefied material (see Figure 11). The behavior in radial velocities confirms that the W4 superbubble is tilted toward the observer and substantiates the formation of a galactic chimney (see Section 5.7).

The dynamical age of the chimney phase is estimated at 4.1 Myr assuming both discontinuities, associated with the wave, to travel with very similar velocities. This implies that the shell opening appeared when the shell's polar cap was roughly located 200 pc above galactic mid-plane (see Section 5.8). In this case, shell instabilities developed in W4 at latitudes well below the blowout threshold, which is between 280 and 420 pc above mid-plane at the distance of the star cluster IC 1805. Magnetohydrodynamic instabilities are likely to have occurred at the earlier stages of the expansion (see Section 5.8). According to a simple model of expanding wind-blown bubbles, roughly 10 Myr was necessary to reach 200 pc and initiate shell fragmentation in W4. Adding the age of the chimney phase, we propose the dynamical age of the superbubble to be approximately 14 Myr (see Section 5.8), a value apparently greater than any previous estimations.

The H I walls do not seem to have a kinematic impact on the vented outflows of ionized material. On the other hand, their inner erosion contributes to the local particle density of particular areas. Otherwise, the fields observed would have enclosed extremely rarefied material which would likely be invisible, according to the model (see Section 5.7).

Our one-dimensional model does not provide indications on how the Hα line widths vary inside a rarefaction wave (see Section 5.2). However, the behavior in line widths can be best explained by a few assumptions regarding the hydrodynamics of the rarefied material and the particular geometry of W4-north. A zone characterized by a dissipation of the turbulence (see Figure 13) could be located immediately behind the southern discontinuity (see Section 5.7). Correlated with the abrupt acceleration observed between Fields 21 and 22 (see Figure 12), the steep line narrowing gradient could be related to a parallelization of the outflows through the top-cap break (see Section 5.7). Collimation could eventually explain the particular kinematic behavior in radial velocities and line widths observed in the northern portion of Field 22. Another scenario demands the northern discontinuity of the wave to be located precisely at the latitude of Field 22; ionized material, that flows through the top-cap break and beyond the zone of rarefaction, might evolve for a certain distance to reach the kinematic configuration of the local DIM material above the superbubble (see Section 5.7). Finally, the particularly low $\beta_{i,\rm corr}$ values in Field 22 indicate a small inclination of the W4 superbubble with respect to the plane of the sky. Using evidence that Discontinuity-N coincides in latitudes with Field 22, we obtain an angle of inclination between 9° and 27° (see Section 5.7).

Using observations in Paper I, we can estimate how much photoeroded material is added per year to the warm ISM enclosed by the H I shell. The rate at which W4-north loses ionized material through the top-cap break is slightly less than this rate. However, the presence of the Hα-poor cavity indicates that the rate of evacuation should clearly dominate. The proposed explanations are mostly associated with geometrical effects: a larger maybe asymmetric top-cap break, a smaller angle of inclination of the superbubble with respect to the plane of the sky, or a sizeable contribution to the evacuation attributed to the western-side break, although the latter is not detected in Hα. Since the uncertainties on each measurement are difficult to quantify, no particular explanation clearly emerges from the others.

The kinematic confirmation of a shell opening near the polar region of W4 signifies that a certain fraction of the UV flux will likely exit the large superbubble through the hole. The formation of a dynamic chimney inside the superbubble/H II region W4 is the evolutionary stage that establishes an energetical connection between the star cluster IC 1805 and the Reynolds loop located at low-galactic corona level.

The authors would like to thank the Natural Sciences and Engineering Research Council of Canada and the Fonds Québécois de la Recherche sur la Nature et les Technologies who provided funds for this research project. The Canadian Galactic

Plane Survey is a Canadian project with international partners and is supported by a grant from the Natural Sciences and Engineering Research Council of Canada. Data from the Canadian Galactic Plane Survey are publicly available through the facilities of the Canadian Astronomy Data Centre (http://www1.cadc-ccda.hia-iha.nrc-cnrc.gc.ca/cgps/).

D.L. is grateful to M.-A. Miville-Deschênes and Olivier Daigle who provided useful IDL routines to carry out data reduction. D.L. would also like to thank B. Malenfant, G. Turcotte and P.-L. Lévesque for technical support during numerous observing nights at the Observatoire du mont Mégantic.

REFERENCES

Atherton, P. D., Taylor, K., Pike, C. D., Harmer, C. F. W., Parker, N. M., & Hook, R. N. 1982, MNRAS, 201, 661
Basu, S., Johnstone, D., & Martin, P. G. 1999, ApJ, 516, 843
Chevalier, R. A., & Gardner, J. 1974, ApJ, 192, 457
Cox, J. P., & Giuli, R. T. 1968, Principles of Stellar Structure (New York: Gordon and Breach), chapter 9
Daigle, O., Carignan, C., Hernandez, O., Chemin, L., & Amram, P. 2006, MNRAS, 368, 1016
de Avillez, M. A., & Berry, D. L. 2001, MNRAS, 328, 708
de Avillez, M. A., & Breitschwerdt, D. 2005, A&A, 436, 585
Dennison, B., Topasna, G. A., & Simonetti, J. H. 1997, ApJ, 474, 31
Dickey, J. M., & Lockman, F. J. 1990, ARA&A, 28, 215
Dove, J. B., Shull, J. M., & Ferrara, A. 2000, ApJ, 531, 846
Dyson, J. E., & Williams, D. A. 1980, The Physics of the Interstellar Medium (Manchester: Manchester Univ. Press), chapter 5
Godbout, S., Joncas, G., & Drissen, L. 1998, PASA, 15, 60
Gol'dfel'd, M. A., Zinov'ev, V. N., & Lebiga, V. A. 1987, Fluid Dynamics, 22, 40
Heiles, C. 1991, IAUS, 147, 43
Hernandez, O., Gach, J.-L., Carignan, C., & Boulesteix, J. 2003, Proc. SPIE, 4841, 1472
Joncas, G., & Roy, J.-R. 1984, ApJ, 283, 640
Lagrois, D., & Joncas, G. 2009, ApJ, 691, 1109 (Paper I)
Landau, L. D., & Lifshitz, E. M. 1987, Fluid Mechanics (2nd ed.; Toronto: Permagon Press), chapter 10
Lenz, D. D., & Ayres, T. R. 1992, PASP, 104, 1104
Lozinskaya, T. A. 1992, Supernovae and Stellar Wind in the Interstellar Medium (New York: AIP), chapter 13
Mac Low, M.-M., & McCray, R. 1988, ApJ, 324, 776
Mac Low, M.-M., McCray, R., & Norman, M. L. 1989, ApJ, 337, 141
Massey, P., Johnson, K. E., & DeGioia-Eastwood, K. 1995, ApJ, 454, 151
Mathis, J. S. 1986, ApJ, 301, 423
McClure-Griffiths, N. M., Ford, A., Pisano, D. J., Gibson, B. K., Staveley-Smith, L., Calabretta, M. R., Dedes, L., & Kalberla, P. M. W. 2006, ApJ, 638, 196
Mizuta, A., Kane, J. O., Pound, M. W., Remington, B. A., Ryutov, D. D., & Takabe, H. 2005, AJ, 621, 803
Norman, C. A., & Ikeuchi, S. 1989, ApJ, 345, 372
Normandeau, M., Taylor, A. R., & Dewdney, P. E. 1996, Nature, 380, 687
Normandeau, M., Taylor, A. R., & Dewdney, P. E. 1997, ApJS, 108, 279
Normandeau, M. 2000, in ASP Conf. Ser., Stars, Gas and Dust in Galaxies: Exploring the Links, ed. D. Alloin, G. Galaz, & K. Olsen (San Francisco, CA: ASP), 221, 41
Osterbrock, D. E., Fulbright, J. P., Martel, A. R., Keane, M. J., Trager, S. C., & Basri, G. 1996, PASP, 108, 277
Reynolds, R. J. 1989a, ApJ, 339, L29
Reynolds, R. J. 1989b, ApJ, 345, 811
Reynolds, R. J., Sterling, N. C., & Haffner, L. M. 2001, ApJ, 558, 101
Shi, H. M., & Hu, J. Y. 1999, A&AS, 136, 313
Shu, F. H. 1992, Gas Dynamics, Vol. II (Mill Valley, CA: University Science Books), chapter 14
Skinner, W. R., Yee, J.-H., Hays, P. B., & Burrage, M. D. 1998, AdSpR, 21, 835
Terebey, S., Fich, M., Taylor, R., Cao, Y., & Hancock, T. 2003, ApJ, 590, 906
Wang, X., & Dalton, C. 1991, International journal for numerical methods in fluids, 12, 383
West, J. L. 2003, Master Thesis, University of Manitoba, Canada
West, J. L., English, J., Normandeau, M., & Landecker, T. L. 2007, ApJ, 656, 914